Hydrol. Earth Syst. Sci. Discuss., 8, 2555–2608, 2011
www.hydrol-earth-syst-sci-discuss.net/8/2555/2011/
doi:10.5194/hessd-8-2555-2011

Hydrology and Earth System Sciences Discussions

Large-scale groundwater modeling using global datasets: a test case for the Rhine-Meuse basin

E. H. Sutanudjaja[1], L. P. H. van Beek[1], S. M. de Jong[1], F. C. van Geer[1,3], and M. F. P. Bierkens[1,2]

[1]Department of Physical Geography, Faculty of Geosciences, Utrecht University, Utrecht, The Netherlands
[2]Deltares, Utrecht, The Netherlands
[3]Netherlands Organization for Applied Scientific Research TNO, Utrecht, The Netherlands

Received: 28 February 2011 – Accepted: 3 March 2011 – Published: 8 March 2011

Correspondence to: E. H. Sutanudjaja (e.sutanudjaja@geo.uu.nl)

Published by Copernicus Publications on behalf of the European Geosciences Union.

Abstract

Large-scale groundwater models involving aquifers and basins of multiple countries are still rare due to a lack of hydrogeological data which are usually only available in developed countries. In this study, we propose a novel approach to construct large-scale groundwater models by using global datasets that are readily available. As the test-bed, we use the combined Rhine-Meuse basin that contains groundwater head data used to verify the model output. We start by building a distributed land surface model (30 arc-second resolution) to estimate groundwater recharge and river discharge. Subsequently, a MODFLOW transient groundwater model is built and forced by the recharge and surface water levels calculated by the land surface model. Although the method that we used to couple the land surface and MODFLOW groundwater model is considered as an offline-coupling procedure (i.e. the simulations of both models were performed separately), results are promising. The simulated river discharges compare well to the observations. Moreover, based on our sensitivity analysis, in which we run several groundwater model scenarios with various hydrogeological parameter settings, we observe that the model can reproduce the observed groundwater head time series reasonably well. However, we note that there are still some limitations in the current approach, specifically because the current offline-coupling technique simplifies dynamic feedbacks between surface water levels and groundwater heads, and between soil moisture states and groundwater heads. Also the current sensitivity analysis ignores the uncertainty of the land surface model output. Despite these limitations, we argue that the results of the current model show a promise for large-scale groundwater modeling practices, including for data-poor environments and at the global scale.

1 Introduction

Groundwater is a vulnerable resource, and in many areas, groundwater is being consumed faster than it is being naturally replenished (e.g. Rodell et al., 2009; Wada et al.,

HESSD

8, 2555–2608, 2011

2010). Given increased population and heightened variability and uncertainty in precipitation due to climate change, the pressure upon groundwater resources is expected to intensify. These issues make monitoring and predicting groundwater changes, especially over large areas, imperative.

Changes in groundwater resources and their causes can be inferred from groundwater models. A groundwater model has the ability to calculate and predict spatio-temporal groundwater head in a sufficiently fine resolution (≤5 km, e.g. Lam et al., 2011). However, large-scale groundwater models, especially for large aquifers and basins of multiple countries, are still rare, mainly due to lack of hydrogeological data. Some existing large-scale models, such as in the Death Valley area, USA (D'Agnese et al., 1999), and in the MIPWA region, the Netherlands (Snepvangers et al., 2007), were developed on the basis of highly detailed information (e.g. elaborate 3-D geological models). Such information may be available in developed countries but is seldom available in other parts of the world.

In this paper, we propose a novel approach for constructing a large-scale groundwater model by using only readily available global datasets. Here the model proposed is a MODFLOW transient groundwater model that is coupled to a distributed land surface model. The latter is used to estimate groundwater recharge and surface water levels that are used to force the groundwater model. As the test bed of this study, we use the combined Rhine-Meuse basin (total area: ±200 000 km^2). This basin, located in Western Europe (see Fig. 1), is selected because it contains ample groundwater head data that can be used to verify the model output. However, while constructing the model, we use only globally available datasets that are listed as follows. We use the Global Land Cover Characteristics Data Base Version 2.0 (GLCC 2.0, http://edc2.usgs.gov/glcc/globe_int.php) and FAO soil maps (1995) in order to parameterize the land cover and upper sub-surface properties. For estimating aquifer hydrogeological properties, we use the lithological map of Dürr et al. (2005), which covers the entire globe, and the UNESCO international hydrogeological map of Europe (http://www.bgr.de/app/fishy/ihme1500/), which is the type of the map that is commonly

HESSD
8, 2555–2608, 2011

available in the other parts of the world. For climatological forcing, we use the global CRU datasets (Mitchell and Jones, 2005; New et al., 2002) that are combined with the ECMWF re-analysis data of ERA-40 (Uppala et al., 2005) and operational archive (http://www.ecmwf.int/products/data/archive/descriptions/od/oper/index.html).

The goal of this paper is then to construct a large-scale groundwater model on the basis of readily available global datasets and to evaluate the model performance using groundwater head observations. Here we do not intend to calibrate the model yet. Rather, we conduct a sensitivity analysis to study how changing aquifer properties influence the model outcome, specifically the resulting groundwater head time series. By this sensitivity analysis, we expect to gain insights into the model behaviour that can be used as the basis for improving the current model.

The paper is organized as follows. In the following section, we explain the model concept and structure used in this study, and how global datasets are used for the model parameterization. Then, we present the methodology to evaluate the model outcome, including the sensitivity analysis procedure. Subsequently, the results and their analyses follow. The last part of this paper is mainly devoted to a discussion about the prospects of large-scale groundwater assessment in data-poor environments and at the global scale, and to suggest ways to further improve this large-scale model.

2 Model concepts, parameterization, and forcing data

2.1 General modeling procedure

The hydrological model developed in this study consists of two parts: (1) the land surface model, which conceptualizes the hydrological processes on and in the upper first meter of the soil layer, and (2) the groundwater model, which describes saturated flow in the deeper underground. The land surface model was adopted from the global hydrology model of PCR-GLOBWB (Van Beek and Bierkens, 2009) having two upper

HESSD
8, 2555–2608, 2011

soil stores and a simple linear groundwater store (see Fig. 2). In this study, we replaced the latter by the MODFLOW groundwater model (McDonald and Harbaugh, 1988).

The model simulation was performed for the period 1960–2008. We started this modeling exercise by modifying PCR-GLOBWB and performing daily simulations to calculate groundwater recharge and river discharge. The river discharge was translated to monthly surface water levels by assuming channel dimensions and properties based on geomorphological relations to bankfull discharge (Lacey, 1930). These surface water levels and groundwater recharge were used to force a weekly transient groundwater model built in MODFLOW. The whole modeling procedure can be considered as an offline-coupling procedure between PCR-GLOBWB and MODFLOW because we separately and sequentially run both of them.

2.2 PCR-GLOBWB land surface model

PCR-GLOBWB is a raster-based global hydrological model coded in the PCRaster scripting languange (Wesseling et al., 1996). It has two upper soil stores and one groundwater store (see Fig. 2). In this Sect. 2.2, we mainly discuss the hydrological processes above and in the first two upper stores, which respectively represent the top 30 cm of soil (thickness $Z_1 \leq 30$ cm) and the following 70 cm of soil ($Z_2 \leq 70$ cm) (in which the storages are respectively symbolized as S_1 and S_2 [L]). In Sect. 2.4, we describe the MODFLOW groundwater model that replaces the groundwater store (S_3).

For a detailed description of PCR-GLOBWB, we refer to Van Beek and Bierkens (2009). Here we briefly describe its main features and report the modifications to the original version of PCR-GLOBWB that were implemented for the purpose of this paper. The original version of PCR-GLOBWB (hereafter called as "PCR-GLOBWB-ORI") has a spatial resolution of 0.5° × 0.5°, while the modified version used in this research (hereafter called as "PCR-GLOBWB-MOD") has 30″ × 30″ grid-cell – approximately equal to 1 km × 1 km grid-cell at the equator. In each cell of both versions (hereafter called as "PCR-GLOBWB"), the states and fluxes are calculated on a daily basis.

HESSD
8, 2555–2608, 2011

Table 5 lists the parameters used in the model. It also contains the global datasets that were used to derive them. The state and flux variables are listed in Table 5. Following Fig. 2, the following paragraphs describe them and how they are modeled.

2.2.1 Interception

PCR-GLOBWB includes a finite interception storage, Si [L], which is subject to evaporation. Precipitation, P [L T^{-1}], which falls either as snow, Sn [L T^{-1}] (if the atmospheric temperature is below the water freezing temperature, $Ta < 0\,^{\circ}$C), or liquid rainfall, P_{rain} [L T^{-1}] (if $Ta \geq 0^{\circ}$C), fills the interception storage up to a certain threshold.

In PCR-GLOBWB-MOD, we use the interception definition as suggested by Savenije (2004), who asserted that interception accounts not only for evaporation from leaf interception, but also any fast evaporation fluxes that occur on the same day as the rainfall as precipitation may be intercepted on many other places, such as rocks, bare soils, roads, urban areas, litters, organic top soil layers, etc. Therefore, the interception capacity is parameterized as:

$$Si_{\text{max,m}} = \left[1 - C_{\text{f,m}}\right] I_{\text{nv}} + C_{\text{f,m}}\, I_{\text{veg}}\, \text{LAI}_{\text{m}} \quad (1)$$

where Si_{max} [L] is the interception capacity of each grid-cell consisting of the fractions C_{f} [–] of vegetation cover. I_{nv} and I_{veg} [L] are parameters defining the interception capacities per unit surface area in non vegetated and vegetated areas. LAI [–] is the leaf area index, commonly defined as the ratio of total upper leaf surface of vegetation divided by the surface area of the land on which the vegetation grows. Equation (1), used in PCR-GLOBWB-MOD, is slightly different than its original version in PCR-GLOBWB-ORI, which limits the interception capacity only to vegetation or leaf canopy represented by the second term of Eq. (1) ($C_{\text{f,m}}\, I_{\text{veg}}\, \text{LAI}_{\text{m}}$). The first term of Eq. (1) ($[1 - C_{\text{f,m}}]\, I_{\text{nv}}$) represents the interception capacity in non vegetated fraction of a grid cell.

The subscript m, which is the monthly index, indicates that Si_{max} shows a monthly or seasonal variation due to vegetation phenology. This seasonal variation is driven by the variations of $C_{\text{f,m}}$ and LAI_{m}, that are assumed to range between the minimum and

HESSD
8, 2555–2608, 2011

maximum values according to growth factors f_m [–]. This growth factor is a function of monthly temperature T_m [Θ]:

$$f_m = 1 - \left(\frac{T_{max} - T_m}{T_{max} - T_{min}}\right)^2 \quad (2)$$

where T_{max} and T_{min} are the maximum and minimum temperatures assumed for the growing and dormancy seasons, and the monthly temperature T_m fields are taken from the 10′ CRU CL 2.0 datasets (New et al., 2002), which contains 12 monthly fields representing the average monthly terrestrial climatology over the period 1961–1990. Using this seasonal growth factor f_m, the seasonal parameters $C_{f,m}$ and LAI_m are subsequently modeled as:

$$LAI_m = LAI_{min} + f_m \times (LAI_{max} - LAI_{min}) \quad (3)$$

$$C_{f,m} = C_{f,min} + f_m \times \left(C_{f,max} - C_{f,min}\right) \quad (4)$$

The maximum and minimum values of LAI and C_f are assigned based on the land cover map of GLCC 2.0 (http://edc2.usgs.gov/glcc/globe_int.php), the global ecosystem classification of Olson (1994a,b), and the improved land surface parameter table of Hagemann (2002). Note that, although T_m, LAI_m, and $C_{f,m}$ show monthly variation, for the sake of simplicity, they have no inter-annual variation so that they represent a climatology over the whole model running period.

The fast evaporation from the intercepted water, E_i [$L\,T^{-1}$], is limited by either available evaporation energy for wet interception areas $E_{p,i}$ [$L\,T^{-1}$] or available water in the interception storage *Si*:

$$E_{p,i} = E_{p,0} \times Kc_i \quad (5)$$

$$E_i\,\Delta t = \min\left(Si,\, E_{p,i}\,\Delta t\right) \quad (6)$$

where $E_{p,0}$ [$L\,T^{-1}$] is the reference potential evaporation energy calculated by the FAO Penman-Monteith method (Allen et al., 1998), Kc_i [–] is the "crop factor" coefficient

HESSD
8, 2555–2608, 2011

assumed for wet interception areas, and Δt [T] is the model simulation timestep, which is one day.

2.2.2 Snow pack

If $Ta < 0\,^{\circ}\mathrm{C}$, the surplus precipitation above the interception capacity $Si_{\max}$ falls as snow and feeds the snow storage, Ss [L], which is modeled with a degree-day-factor (DDF [$\mathrm{L\,\Theta^{-1}\,T^{-1}}$]) method adapted from the HBV model (Bergström, 1995). Snow may melt (if $Ta \geq 0\,^{\circ}\mathrm{C}$) and melt water may refreeze with linear rate CFR [$\mathrm{T^{-1}}$] (if $Ta < 0\,^{\circ}\mathrm{C}$) or evaporate (if enough energy is available). Melt water can also be stored in a storage Ss_{l} [L] up to a certain maximum holding capacity that is proportionally related to actual snow storage and controlled by a factor CWH [–]. Any surplus above this holding capacity is transferred to the soil.

2.2.3 Direct or surface runoff

If $Ta \geq 0\,^{\circ}\mathrm{C}$, the net input flux transferred to the soil P_{n} [$\mathrm{L\,T^{-1}}$] consists of the surplus precipitation above the interception capacity $Si_{\max}$ (falling as liquid rainfall) and excess melt water from the snow pack. In principle, P_{n} infiltrates if the soil is not saturated and causes direct runoff if the soil is saturated. However, this principle cannot be straightforwardly implemented because we have to account for the variability of soil saturation within a $30'' \times 30''$ cell. Here we adopted the Improved Arno Scheme (Hagemann and Gates, 2003), in which the total soil water storage capacity of a cell consists of the aggregate of many different soil water storage capacities. Following this scheme, the fraction of saturated soil x is given by:

$$x = 1 - \left(\frac{w_{\max} - w_{\mathrm{act}}}{w_{\max} - w_{\min}} \right)^{\mathrm{b}} \tag{7}$$

where $w_{\max}$ and $w_{\min}$ [L] ares the maximum and minimum local sub-grid soil water capacities, w_{act} [L] is the actual local sub-grid soil water storage that corresponds to

HESSD
8, 2555–2608, 2011

the fractional saturation of a grid, x [–], and b [–] is a dimensionless shape parameter that defines the distribution of w_{act} between w_{max} and w_{min}.

For PCR-GLOBWB, instead of using the local sub-grid values w, Van Beek and Bierkens (2009) have translated the Improved Arno Scheme in terms of grid-average values W [L]:

$$x = 1 - \left(\frac{W_{max} - W_{act}}{W_{max} - W_{min}}\right)^{\frac{b}{b+1}} \quad (8)$$

where W_{max} is the grid-average capacity, W_{min} ($= w_{min}$) is the minimum capacity, and W_{act} is the grid-average actual soil storage. Because PCR-GLOBWB consists of two upper soil storages, the grid-average actual soil storage and capacity are calculated as $W_{act} = S_1 + S_2$ and $W_{max} = SC_1 + SC_2$, where SC [L] is the soil water capacity for each each layer. Based on the scheme of Eq. (8), the net input flux P_n and soil storage W_{act} are divided into direct runoff, Q_{dr} [$L\,T^{-1}$], and infiltration flux into the first soil layer, P_{01} [$L\,T^{-1}$]. The direct runoff is given by:

$$Q_{dr}\,\Delta t = \begin{cases} 0 & \text{if } P_n\,\Delta t + W_{act} \le W_{min} \\ P_n\,\Delta t - (W_{max} - W_{act}) + \Delta W\left[\left(\frac{W_{max} - W_{act}}{\Delta W}\right)^{\frac{1}{b+1}} - \frac{P_n\,\Delta t}{(b+1)(\Delta W)}\right]^{b+1} & \text{if } W_{min} < P_n\,\Delta t + W_{act} \le W_{max} \\ P_n\,\Delta t - (W_{max} - W_{act}) & \text{if } P_n\,\Delta t + W_{act} > W_{max} \end{cases} \quad (9)$$

where $\Delta W = W_{max} - W_{min}$.

Equation (9) states that an event P_n, for a given cell and a given period Δt, only generates runoff Q_{dr} if it brings the grid-average actual soil storage W_{act} above the grid-minimum soil capacity W_{min}. It implies that W_{min} is an important parameter governing runoff generation response time, especially for large and highly variability grid cells that are usually used in PCR-GLOBWB-ORI, with a spatial resolution of 0.5° × 0.5°. However, for relatively small cells in PCR-GLOBWB-MOD, with a spatial resolution of

HESSD
8, 2555–2608, 2011

$30'' \times 30''$, W_{min} is less important. Therefore, for the sake of simplicity, we took W_{min} equal to 0 for all cells of PCR-GLOBWB-MOD.

However, we still consider the influence of elevation variability in a $30'' \times 30''$ cell, particularly by the existence of parameter b that accounts for the fact that, for a given cell-average soil wetness, we expect more runoff is produced in mountainous regions than in flat regions (see e.g., Hagemann and Gates, 2003):

$$b = \max\left(\frac{\sigma_h - \sigma_{min}}{\sigma_h + \sigma_{max}}, 0.01\right) \quad (10)$$

where σ_h is the standard deviation of orography within a $30'' \times 30''$ cell calculated from the 3-arc-second topography dataset HydroSHEDS, σ_{min}, and σ_{max} are the model-area minimum and maximum standard deviations of orography at the grid resolution.

Through this scheme, the amount of infiltration P_{01} transferred to the first soil store is equal to the difference between P_n and Q_{dr} ($P_{01} = P_n - Q_{dr}$). However, we also have to consider that the infiltration rate cannot exceed the saturated hydraulic conductivity of the first layer, $k_{sat,1}$ [$L\,T^{-1}$]. In this case, if $P_{01} > k_{sat,1}$, its excess is passed to the direct runoff Q_{dr}.

2.2.4 Vertical water exchange between soil and groundwater stores

The net vertical flux between the first and second storages, Q_{12} [$L\,T^{-1}$], is driven by the degrees of saturation of the both layers, s [–], that can be calculated as $s_1 = S_1/SC_1$ and $s_2 = S_2/SC_2$. By definition, s can also be expressed as $s_1 = \theta_1/\theta_{sat,1}$ and $s_2 = \theta_2/\theta_{sat,2}$, where the subscript sat indicates the saturation condition and θ [–] is the effective soil moisture content that can also be expressed as the fraction of soil storage over soil thickness ($\theta_1 = S_1/Z_1$ and $\theta_2 = S_2/Z_2$).

In principle, the net vertical flux Q_{12} may consist of a downward percolation $Q_{1\to2}$ [$L\,T^{-1}$], and a capillary rise $Q_{2\to1}$ [$L\,T^{-1}$]. If there is enough water in S_1, the percolation $Q_{1\to2}$ is equal to the first store unsaturated hydraulic conductivity, $k_1(s_1)$ [$L\,T^{-1}$]. If

HESSD
8, 2555–2608, 2011

$s_1 < s_2$, capillary rise may occur with the amount of $Q_{2\rightarrow1} = k_2(s_2) \times (1 - s_1)$, where $k_2(s_2)$ [$\mathrm{L\,T^{-1}}$] is the second store unsaturated hydraulic conductivity and $(1 - s_1)$ is the moisture deficit in the first store. The unsaturated hydraulic conductivity of each layer, $k(s)$, which depend on the degree of saturation s, is calculated based on the relationship suggested by Campbell (1974):

$$k(s) = k_{\mathrm{sat}} \times s^{2\beta+3} \tag{11}$$

where k_{sat} [$\mathrm{L\,T^{-1}}$] is the saturated hydraulic conductivity and β [–] is an empirical exponent for a soil water retention curve fitted based on the model of Clapp and Hornberger (1978):

$$\psi = \psi_{\mathrm{sat}} \times s^{-\beta} \tag{12}$$

where ψ is the soil matric suction [L]. Equations (11) and (12) are used for both soil stores. We removed the subscripts 1 and 2, that should have indicated the first and second stores, only for the sake of simplicity. To assign all soil parameter (i.e. β, k_{sat}, ψ_{sat}, θ_{sat} and Z – see Table 5), we used the FAO soil map (1995) and a soil parameter table that was derived by Van Beek and Bierkens (2009) based on the database of Global Soil Data Task (2000).

The net vertical flux between the second store and third or groundwater store, Q_{23} [$\mathrm{L\,T^{-1}}$], also consists of the downward percolation $Q_{2\rightarrow3}$ [$\mathrm{L\,T^{-1}}$] and the capillary rise $Q_{3\rightarrow2}$ [$\mathrm{L\,T^{-1}}$]. Similarly, $Q_{2\rightarrow3}$ [$\mathrm{L\,T^{-1}}$] is controlled by the unsaturated hydraulic conductivity of the corresponding storage ($k_2(s_2)$) as well as the groundwater level. However, in PCR-GLOBWB-MOD, to force one-way coupling of the land surface model and MODFLOW (see the beginning part of the Sect. 2.1), we set the capillary rise from the groundwater to soil stores ($Q_{3\rightarrow2} = 0$) to zero, which is one of the limitations of the current modeling approach.

HESSD
8, 2555–2608, 2011

2.2.5 Interflow or shallow sub-surface flow

In shallow soil deposits covering bed rocks and in regolith soil developed in mountainous areas, interflow or sub-surface storm flow is an important runoff component as perched groundwater bodies usually occur during wet periods. In PCR-GLOBWB, we model the interflow, Q_{sf} [L T^{-1}], as releasing water from the second store based on a simplified approach of Sloan and Moore (1984):

$$LQ_{sf}(t) = \left[1 - \frac{\Delta t}{\mathrm{TCL}}\right] LQ_{sf}\,(t - \Delta t) + \frac{\Delta t}{\mathrm{TCL}}\, L\, \left[Q_{12}(t) - Q_{23}(t)\right] \quad (13)$$

where (t) and $(t - \Delta t)$ indicate the actual time and previous time, $LQ_{sf}(t)$ [L^2 T^{-1}] is the interflow per unit hillslope width, and L [L] is the average length of overland flow or hillslope length. The latter is defined as half the average distance between stream channels. The parameter TCL [T] is a characteristic response time that is given by:

$$\mathrm{TCL} = \frac{L \times \left(\theta_{sat,2} - \theta_{fc,2}\right)}{2 \times k_{sat,2} \tan\left(\alpha\right)} \quad (14)$$

where $\tan(\alpha)$ [–] is the grid-average slope for each $30'' \times 30''$ cell and θ_{fc} [–] is the effective the soil moisture content at field capacity. To derive the latter, we used Eq. (12) and assumed the matric suction ψ_{fc} (at field capacity) equals 1 m.

The topography related parameters in Eq. (14), $\tan(\alpha)$ and L, were derived from the 3-arc second dataset of HydroSHEDS (Lehner et al., 2008). To get the hillslope length L, we derived the channel network map of the Rhine-Meuse basin using the 3-arc second digital elevation and drainage direction maps of HydroSHEDS. First, we calculated a generalized divergence map ∇s (a generalized curvature) using 3×3 moving windows as outlined by Zevenbergen and Thorne (1987). Subsequently, by tracking from the most upstream 3-arc second cells, we located "channel head" cells, which are the inflection points from hillslope landscape cells – that are dominated by mass wasting and generalized by positive ∇s – to valley cells – that are areas of topographic convergence and generalized by negative ∇s (Montgomery and Foufoula-Georgiou, 1993;

HESSD
8, 2555–2608, 2011

Howard, 1994). Furthermore, we assumed every cell located downstream of these channel head cells to have streams with the length equal to its cell diagonal length. Considering errors that may exist in the digital elevation model, we added the criteria that cells that have drainage contributing area higher than 2500 of 3-arc second cells (about 25 km^2 at the equator) are channeled cells. Having derived the channel network map, we can calculate the hillslope length L, which is approximately equal to half the reciprocal of drainage density, $1/2D$ (see for example Rodriguez-Iturbe and Rinaldo, 1997).

2.2.6 Soil evaporation and plant transpiration

Soil evaporation, Es [$L\,T^{-1}$], may originate from two places: (1) from the first soil store (in which the storage is S_1) and (2) from the melt water store in the snow pack (Ss_l). The evaporation flux from Ss_l, which is symbolized by Es_l [$L\,T^{-1}$], is always prioritized over that from S_1, which is symbolized by Es_1 [$L\,T^{-1}$]. The total flux of both is limited by the potential evaporation energy left after interception evaporation flux, $E_{p,s}$ [$L\,T^{-1}$] ($Es_{sl} + Es_1 \le E_{p,s}$). In addition, the evaporation flux Es_1 in the saturated area x is limited by the saturated hydraulic conductivity $k_{sat,1}$, while the one in the unsaturated area $(1-x)$ is limited by the unsaturated hydraulic conductivity $k_1(s_1)$. In PCR-GLOBWB-MOD, the aforementioned principles are summarized by:

$$E_{p,s} = \left(E_{p,0} - f_i\,E_i\right) \times Kc_s \times (1 - C_f) \tag{15}$$

$$Es_l\,\Delta t = \min\left(Ss_l,\, E_{p,s}\,\Delta t\right) \tag{16}$$

$$Es_1 = x \times \min\left(k_{sat,1},\, E_{p,s} - Es_l\right) + (1-x) \times \min\left[k_1(s_1),\, E_{p,s} - Es_l\right] \tag{17}$$

where f_i [–] is a parameter for updating $E_{p,0}$ [$L\,T^{-1}$] after the interception flux E_i (taken as 1) and Kc_s [–] is a "crop factor" coefficient assumed for bare soil area.

Transpiration occurs due to root abstraction from both first and second soil stores. The total transpiration flux T_{12} [$L\,T^{-1}$] is limited to the potential energy left for transpiration after energy used for interception evaporation flux, $E_{p,T}$ [$L\,T^{-1}$] (hereafter called

HESSD
8, 2555–2608, 2011

as potential transpiration). It is also limited to total available water in both storages, $S_1 + S_2$. Under fully saturated conditions, roots can experience lack of aeration that prevents themselves to uptake water. Therefore, we consider that transpiration only takes place in unsaturated area $(1 - x)$ and depends on the total available moisture in the soil layer. In PCR-GLOBWB-MOD, the aforementioned principles are summarized by:

$$E_{p,T} = \left(E_{p,0} - f_i E_i\right) K c_T C_f \tag{18}$$

$$T_{12} = f_T E_{p,T} (1 - x) \tag{19}$$

where $K c_T$ [−] is the crop factor coefficient assumed for each land cover type and f_T [−] is a factor to reduce the transpiration because of lack of soil moisture (water stress) that was derived by Van Beek and Bierkens (2009) following the Improved Arno Scheme concept:

$$f_T = \frac{1}{1 + \left(\theta_E / \theta_{50\%}\right)^{-3\,\beta_{50\%}}} \tag{20}$$

$$\theta_E = \frac{W_{max} + b(W_{max} - W_{min}) \left[1 - \frac{b+1}{b} \left(\frac{W_{max} - W_{act}}{(W_{max} - W_{min})}\right)^{\frac{1}{b+1}}\right]}{W_{max} + b\,(W_{max} - W_{min}) \left[1 - \left(\frac{W_{max} - W_{act}}{(W_{max} - W_{min})}\right)^{\frac{1}{b+1}}\right]} \tag{21}$$

where $\theta_{50\%}$ [−] and $\beta_{50\%}$ [−] are the degree of saturation at which the potential transpiration is halved and the corresponding coefficient of the soil water retention curve. θ_E [−] is the average degree of saturation over the unsaturated fraction $(1 - x)$. Note that all θ_E, $\theta_{50\%}$ and $\beta_{50\%}$ are effective values for the entire first and second soil stores. While θ_E is a state variable that changes over time, both $\theta_{50\%}$ and $\beta_{50\%}$ are model parameters estimated by:

$$\theta_{50\%} = \frac{SC_1 R_{f,1} \left(\psi_{50\%} / \psi_{sat,1}\right)^{-1/\beta} + SC_2 R_{f,2} \left(\psi_{50\%} / \psi_{sat,2}\right)^{-1/\beta}}{SC_1 R_{f,1} + SC_2 R_{f,2}} \tag{22}$$

HESSD
8, 2555–2608, 2011

$$\beta_{50\%} = \frac{SC_1\, R_{f,1}\, \beta_1 + SC_2\, R_{f,2}\, \beta_2}{SC_1\, R_{f,1} + SC_2\, R_{f,2}} \quad (23)$$

where the subscripts 1 and 2 indicate the first and second soil layers, $\psi_{50\%}$ [L] is the matric suction at which potential transpiration is halved (taken as 3.33 m), and R_f [–] is the root fractions per soil layer. Here, for the sake of simplicity, we assumed that the root fractions are proportionally distributed according to the layer thicknesses, $R_{f,1} = Z_1/(Z_1 + Z_2)$ and $R_{f,2} = Z_2/(Z_1 + Z_2)$.

The distribution of the total transpiration T_{12} to the fluxes from both stores, T_1 and T_2 [$L\,T^{-1}$], is based on the root fractions, $R_{f,1}$ and $R_{f,2}$, and available water storages, S_1 and S_2:

$$T_1 = \frac{R_{f,1}\, S_1}{R_{f,1}\, S_1 + R_{f,2} S_2} \times T_{12} \quad (24)$$

$$T_2 = \frac{R_{f,2}\, S_2}{R_{f,1} S_1 + R_{f,2} S_2} \times T_{12} \quad (25)$$

Within a time step, the transpiration fluxes have the same priority as the other fluxes leaving the soil stores. T_1 has the same priority as Es_1 and Q_{12}, while T_2 has the same priority as Q_{12} and Q_{sf}. If the available storage to accommodate all fluxes is limited, each flux is reduced proportionally to their size.

Crop factors Kc_T [–] in Eq. (18), assumed based on land cover types, are calculated in the following way (Allen et al., 1998):

$$Kc_{T,m} = Kc_{min} + \left[Kc_{full} - Kc_{min}\right] \times \left[1 - \exp\left(-0.7\, LAI_m\right)\right] \quad (26)$$

where Kc_{min} and Kc_{full} are assumed crop factors under bare minimum and full vegetation cover conditions. The first was taken as 0.2, while the latter was obtained by Allen et al. (1998):

$$Kc_{full} = 1.0 + 0.1 \times h_{veg} \leq 1.2 \quad (27)$$

HESSD
8, 2555–2608, 2011

where h_{veg} is the height of vegetation in meter based on the table defined by Van Beek (2008).

2.2.7 Baseflow and specific runoff from a land surface cell

In the land surface model part of PCR-GLOBWB-MOD, we still used the groundwater linear reservoir (in which the storage is S_3 [L]) in order to calculate the baseflow component Q_{bf} [$L\,T^{-1}$] of the total runoff:

$$Q_{bf} = S_3\,J \tag{28}$$

where J [T^{-1}] the a reservoir coefficient, the reciprocal of which represents the average residence time in the groundwater store. The parameter J is parameterized based on Kraaijenhoff van de Leur (1958):

$$J = \frac{\pi^2 (kD)}{4\,Sy\,L^2} \tag{29}$$

where (kD) [$L^2\,T^{-1}$] is the aquifer transmissivity and Sy [–] is the aquifer porosity or storage coefficient. To parameterize J, we used several globally available datasets that are evaluated with a MODFLOW groundwater model (see Sect. 2.4.1).

From the three flow components, Q_{dr}, Q_{sf}, and Q_{bf}, we can calculate the local runoff, Q_{loc} [$L\,T^{-1}$] in each land surface cell as follows:

$$Q_{loc} = Q_{dr} + Q_{sf} + Q_{bf} \tag{30}$$

Note that Eq. (30) is not valid for "surface water" cells, in which the conceptualization is described in the Sect. 2.2.8. Moreover, for cells with "urban" and "glacier ice" land cover types, Q_{loc} consists of only direct runoff Q_{dr} because those cells are considered as impermeable areas where no infiltration into the soil can occur.

It is also important to note that contrary to the $30' \times 30'$ cells in PCR-GLOBWB-ORI, a $30'' \times 30''$ cell in PCR-GLOBWB-MOD has a single and uniform type of land cover,

HESSD
8, 2555–2608, 2011

vegetation and soil. There are no sub-grid variability of land cover, vegetation and soil types. However, sub-grid elevation variability, which is important for surface runoff generation, interflow and evaporation, is considered in PCR-GLOBWB-MOD (based on the DEM of HydroSHEDS, see Eq.10).

2.2.8 Surface water bodies and surface water accumulation in the land surface model

For cells classified as surface water bodies, we assumed that the local storage change Q_{wat} [$L\,T^{-1}$] is only influenced by the precipitation P and open water evaporation, E_{wat} [$L\,T^{-1}$]:

$$Q_{wat} = P - E_{wat} \tag{31}$$

where E_{wat} is calculated as:

$$E_{wat} = E_{p,0} \times Kc_{wat} \tag{32}$$

with Kc_{wat} [–] is the "crop factor" coefficient assumed for surface water bodies.

Knowing the cell areas for all grid-cells, A_{cell} [L^2], and combining the local specific runoff from the surface water bodies Q_{wat} and from the land surface cells Q_{loc}, we can express the total local runoff in a water volume per unit time Q_{tot} [$L^3\,T^{-1}$]:

$$Q_{tot} = A_{cell} \times \left[(1 - f_{wat})\,Q_{loc} + f_{wat}\,Q_{wat}\right] \tag{33}$$

where f_{wat} [–] is either one for surface water cells or zero for non-surface water cells. To get a f_{wat} map, we integrated the surface water bodies identified in the GLCC 2.0 land cover map and the levels 1 and 2 of the Global Lakes and Wetlands Database (Lehner and Döll, 2004).

In this study, we limited the discharge calculation to monthly resolution. Therefore, we could neglect water residence time in channels (less than a week) and obtain monthly discharge time series Q_{chn} [$L^3\,T^{-1}$] by simply accumulating the monthly values of Q_{tot} along the drainage network based on HydroSHEDS. Latter, these monthly time series Q_{chn} were used to force the MODFLOW groundwater model.

HESSD
8, 2555–2608, 2011

2.3 Climatological forcing data

Climatological forcing time series maps, consisting of temperature *Ta*, precipitation P, and potential evaporation $E_{p,0}$, were supplied on a daily basis. We used the monthly CRU dataset (Mitchell and Jones, 2005; New et al., 2002) in combination with the EMCWF ERA-40 re-analysis data (Uppala et al., 2005), for the period 1960–1999, and the EMCWF operational archive (http://www.ecmwf.int/products/data/archive/descriptions/od/oper/index.html), for the period 2000–2008.

2.3.1 Period 1960–1999

For the period 1960–1999, we used the monthly CRU-TS2.1 dataset (Mitchell and Jones, 2005), which contains time series between 1901 to 2002, and the daily ERA-40 reanalysis dataset (Uppala et al., 2005), which covers the period 1957–2002. We started by re-sampling all ERA-40 maps into maps with half-degree resolution, which is also the spatial resolution of CRU-TS2.1. The ERA-40 daily time series that have been re-sampled were subsequently used to downscale the monthly CRU-TS 2.1 into daily values. To obtain even finer spatial resolution maps, we used the 10-min resolution CRU-CL2.0 dataset (New et al., 2002), which contains 12 monthly fields representing the average monthly terrestrial climatology over the period 1961–1990.

For precipitation P, the downscaling algorithm is summarized by:

$$P_{30',\mathrm{d}} = \frac{P_{\mathrm{ERA-40,\ 30,d}}}{P_{\mathrm{ERA-40,\ 30',m}}} \times P_{\mathrm{CRU-TS2.1,30',m}} \tag{34}$$

$$P_{\mathrm{f},10',\mathrm{d}} = \frac{P_{\mathrm{CRU-CL2.0,10',m}}}{P_{\mathrm{CRU-CL2.0,30',m}}} \times P_{30',\mathrm{d}} \tag{35}$$

where the subscripts $10'$ and $30'$ indicate the map spatial resolutions, the subscripts m and d indicate the monthly and daily temporal resolutions, the subscripts CRU-CL2.0,

HESSD
8, 2555–2608, 2011

CRU-TS2.1, and ERA-40 indicate the dataset names, while the subscript f stands for the final or derived forcing data that are supplied to the land surface model.

Equation (34), used for temporal downscaling from monthly to daily fields, and Eq. (35), used for spatial downscaling from 30′ to 10′ fields, were also used to derive the daily 10′ forcing temperature data $Ta_{10',d}$. For this temperature downscaling, the unit must be in Kelvin (K) in order to avoid zero or near zero values in the denominators. To improve the spatial resolution of the snow coverage during the snow pack simulation, we decided to increase $Ta_{10',d}$ to 30″ resolution, $Ta_{f,30'',d}$, by introducing the temperature lapse rate, T_{LR} [ΘL^{-1}]:

$$Ta_{f,30'',d} = Ta_{10',d} + T_{LR} \times (DEM_{30''} - DEM_{10'}) \quad (36)$$

where $DEM_{30''}$ [L] is taken from the 30″ digital elevation map of HydroSHEDS (Lehner et al., 2008) and $DEM_{10'}$ [L] is its aggregated version at 10′ resolution.

For the monthly reference potential evaporation $E_{p,0}$ fields, we used the dataset derived by Van Beek (2008), which are at 30′ resolution, covering the period 1901–2002 and derived using the FAO Penman-Monteith (Allen et al., 1998). To derive these fields, Van Beek used relevant climatological fields from the CRU-TS2.1 datasets, such as cloud cover, vapour pressure, and average, minimum and maximum temperature. Because there are no wind speed fields defined in the CRU-TS2.1 datasets, Van Beek employed the CRU-CL1.0 (New et al., 1999) dataset, which contains average monthly terrestrial wind speed over the period 1961–1990.

For PCR-GLOBWB-MOD, the monthly reference potential evaporation fields of Van Beek (2008), symbolized as $E_{p,0,*,30',m}$, were downscaled into 10' resolution fields using the monthly CRU-CL2.0 temperature, $Ta_{CRU-CL2.0,30',m}$ (in K) and into daily resolution by using the daily 10' forcing temperature data, $Ta_{f,10',d}$ (K). The algorithm is summarized by:

$$E_{p,0,f,10',m} = \frac{Ta_{CRU-CL2.0,10',m}}{Ta_{CRU-CL2.0,30',m}} \times E_{p,0,*,30',m} \quad (37)$$

HESSD
8, 2555–2608, 2011

$$E_{p,0,f,10',d} = \frac{Ta_{f,10',d}}{Ta_{f,10',m}} \times E_{p,0,f,10',m} \quad (38)$$

2.3.2 Period 2000–2008

For the precipitation and temperature forcing data during the period 2000–2008, we used the other dataset derived by Van Beek (personal communication, 2009), who used the ECMWF operational archive datasets (http://www.ecmwf.int/products/data/archive/descriptions/od/oper/index.html) that were constrained to the long term averages and trends of the CRU-TS2.1 datasets as follows:

1. For each year y, the annual mean of the CRU-TS2.1 forcing data, $F_{CRU-TS2.1,y}$ (which may be either precipitation or temperature), was calculated. Subsequently, the long term mean of $F_{CRU-TS2.1,y}$ for the period 1961–1980 – symbolized as $\bar{F}_{CRU-TS2.1,1961-1980}$ – was calculated.
2. Next, for the period 1981–2002, Van Beek calculated the anomaly time series A_y, which are the anomaly of $F_{CRU-TS2.1,y}$ against $\bar{F}_{CRU-TS2.1,1961-1980}$ ($A_y = F_{CRU-TS2.1,y} - \bar{F}_{CRU-TS2.1,1961-1980}$).
3. Furthermore, the trend of the A_y time series was regressed with the following linear model:

$$A_y^{trend} = b_0 + b_1 \times y \quad (39)$$

where A_y^{trend} is the dependent variable predicted by the linear model, while b_0 and b_1 are the intercept and slope parameters.

4. Subsequently, the long term mean over the period 2000–2008, $\bar{F}^{trend}_{CRU-TS2.1,2000-2008}$, was estimated using Eq. (39), $\bar{F}_{CRU-TS2.1,1961-1980}$ and the year y = 2004, which is taken as the representative for the period 2000–2008:

$$\bar{F}^{trend}_{CRU-TS2.1,2000-2008} = \bar{F}_{CRU-TS2.1,1961-1980} + (b_0 + b_1 \times 2004) \quad (40)$$

HESSD
8, 2555–2608, 2011

5. As done in the step 1, the average of annual means of the ECMWF operational archive datasets (hereafter called as "ECMWF-OA") for the period 2000–2008 – symbolized as $\bar{F}_{\mathrm{ECMWF-OA,2000-2008}}$ – was also calculated.

6. Next, the bias between $\bar{F}_{\mathrm{ECMWF-OA,2000-2008}}$ and $\bar{F}^{\mathrm{trend}}_{\mathrm{CRU-TS2.1,2000-2008}}$, was identified and used to correct the ECMWF operational archive datasets:

$$F_{\mathrm{ECMWF-OA-corr,m}} = F_{\mathrm{ECMWF-OA,m}} + \left(\bar{F}^{\mathrm{trend}}_{\mathrm{CRU-TS2.1,2000-2008}} - \bar{F}_{\mathrm{ECMWF-OA,2000-2008}}\right) \quad (41)$$

where $F_{\mathrm{ECMWF-OA,m}}$ are the original monthly ECMWF-OA data and $F_{\mathrm{ECMWF-OA-corr,m}}$ are their corrected monthly data that would be used to force the land surface model (for the period 2000–2008).

7. The aforementioned procedure is done at monthly and $30'$ resolutions for both precipitation P and temperature Ta fields. To obtain finer resolutions, Eqs. (34) and (35) were used to downscale to daily and $10'$ resolutions.

To obtain monthly reference potential evaporation $E_{\mathrm{p,0}}$ fields over the period 2000–2008, for most of which no CRU datasets are available, Van Beek (personal communication, 2009) defined a procedure to select the corresponding data from his $E_{\mathrm{p,0,*,30',m}}$ dataset (that covers the period 1901-2002). The procedure – repeated for every $30' \times 30'$ grid-cell, for every month and for every year (between the period 2000–2008) – is summarized as follows:

1. For the same month m, Van Beek identified from the CRU-TS2.1 datasets (covering the period 1901–2002) the best corresponding year y–CRU in that the precipitation $P_{\mathrm{CRU-TS2.1,m,y-CRU}}$ and temperature $Ta_{\mathrm{CRU-TS2.1,m,y-CRU}}$ are similar to $P_{\mathrm{ECMWF-OA-corr,m,y}}$ and monthly temperature $Ta_{\mathrm{ECMWF-OA-corr,m,y}}$. Note that both $P_{\mathrm{ECMWF-OA-corr,m,y}}$ and $Ta_{\mathrm{ECMWF-OA-corr,m,y}}$ are the corrected monthly ECMWF-OA data (see Eq. 41).

HESSD
8, 2555–2608, 2011

2. Subsequently, it is assumed that the monthly reference potential evaporation $E_{p,0,2000-2008,30',m,y}$ is the same as the monthly reference potential evaporation of Van Beek (2008) for the month m and year y−CRU, $E_{p,0,*,m,y-CRU}$.

3. To get finer resolutions, Eqs. (37) and (38) were used in order to downscale to 10 arc-min and daily resolutions.

2.4 Groundwater model

As mentioned earlier, a MODFLOW based groundwater model is used to replace the groundwater store S_3 in the land surface model. Here we built a simple MODFLOW model that considers only a single upper aquifer (see Sect. 2.4.1). The MODFLOW model was forced by the output of PCR-GLOBWB-MOD, particularly the monthly recharge Q_{23} (see Sect. 2.4.2) and the monthly channel discharge Q_{chn} that is beforehand translated to surface water levels (see Sect. 2.4.3). We performed groundwater flow simulation for the period 1965–2008 using a weekly time step and monthly stress period, within which specific groundwater recharge and surface water levels are constant.

2.4.1 Aquifer properties

To characterize the properties of the upper aquifer, we initially turned to the global lithological map of Dürr et al. (2005) and the UNESCO international hydrogeological map of Europe (http://www.bgr.de/app/fishy/ihme1500/). However, both maps are inaccurate at the 30″ resolution employed here. The first map does not include small aquifer features that are often located in narrow valleys. Moreover, the locality of units is not accurate at 30″ resolution, particularly after being checked with the digital elevation map $DEM_{30''}$ that we used. Although the latter map includes small features, it is as yet only a scanned map (not a digital one) with all its geocoding problems.

To overcome these difficulties, we developed a procedure that classifies the model area to shallow permeable sedimentary basin aquifers and deep less permeable

HESSD
8, 2555–2608, 2011

mountainous aquifers. The method uses the digital elevation map $DEM_{30''}$ and a steady-state MODFLOW groundwater model:

1. First, for the entire model area, we assumed a set of uniform aquifer properties, $kD = 100\,m^2\,day^{-1}$ and $Sy = 0.25$, specifically for calculating the groundwater recession coefficient J in Eq. (29) of the land surface model.

2. Next, we ran the PCR-GLOBWB-MOD land surface model for a long period (e.g. 1960–2008).

3. Subsequently, using the output of step 2, the average recharge and discharge fields were calculated. The latter was translated to surface water level fields by using relations between discharge and channel dimensions (see Sect. 2.4.3).

4. The average water level and discharge fields derived in the step 3 were used to force the groundwater model in order to estimate the steady-state groundwater head field. Furthermore, using the $DEM_{30''}$, the steady-state groundwater depth d_{gw} could also be derived.

5. We assumed that cells with steady-state groundwater depths d_{gw} of less than 25 m to be productive aquifers. These shallow groundwater table cells, located in valleys, were classified as the "sedimentary basin" class. To avoid the occurrence of isolated cells due to errors in the $DEM_{30''}$, we used the $LDD_{30''}$ to assure that downstream cells of a sedimentary basin cell are also classified as sedimentary basin cells. Moreover, we also made sure that a sedimentary basin cell must have at least one neighbor in its left, right, upper, or lower extents. This is done in order to ensure flow connectivity because MODFLOW uses a discretization that does not allow diagonal flow across the corners (see e.g., Wolf et al., 2008).

6. The remaining cells were subsequently classified as "mountainous area" cells, where groundwater bodies are most likely located at greater depths. Note that here we mean real groundwater bodies, not perched groundwater storage in regolith, which are modeled in the interflow module of the land surface model.

HESSD
8, 2555–2608, 2011

7. For the sedimentary basin class, we assigned a relatively high transmissivity and porosity ($kD = 100\,m^2\,day^{-1}$ and $Sy = 0.25$), while a relatively low transmissivity and porosity is assigned for the mountainous area class ($kD = 25\,m^2\,day^{-1}$ and $Sy = 0.02$).

8. Using the aquifer properties defined in the step 7, we repeated steps 2–7 to approximate the steady-state groundwater depth (shown in Fig. 3) and to subsequently define the final classification map, that was verified with the UNESCO international hydrogeological map of Europe (http://www.bgr.de/app/fishy/ihme1500/), and its kD and Sy fields.

The fields of kD and Sy were stored in the "Block-Centered Flow" (BCF) package of MODFLOW. Here we defined a single aquifer layer with constant kD and Sy for the entire simulation. Note that special attention is needed to defining the storage coefficient Sy for MODFLOW, which normally uses a rectangular discretization with appropriate unit lengths (e.g. m). In MODFLOW (specifically the BCF package that we used), the input values of Sy are commonly multiplied by the cell areas to create so-called "storage capacities" ($SC_{MODFLOW}$, unit: m^2) that are stored and used for MODFLOW calculation (see McDonald and Harbaugh, 1988, Chapter 5). The MODFLOW groundwater model that we built has the same resolution as the land surface model: $30'' \times 30''$. It means that our MODFLOW cells, which are not rectangular, have inappropriate length units and varying surface areas A_{cell} (m^2). Given this fact, we have to modify the input of Sy so that $SC_{MODFLOW}$ has correct values and units:

$$Sy_{inp} = Sy_{act} \times \frac{A_{cell}}{(30'' \times 30'')} \quad (42)$$

where Sy_{inp} is the input values that are supplied to the BCF package of MODFLOW and Sy^{act} are the actual values of storage coefficients. Using these Sy_{inp} input values, the values of $SC_{MODFLOW}$, internally multiplied by the cell length ($30'' \times 30''$) in the BCF package, are:

HESSD
8, 2555–2608, 2011

$$SC_{\text{MODFLOW}} = Sy_{\text{inp}} \times (30'' \times 30'') \tag{43}$$

$$SC_{\text{MODFLOW}} = Sy_{\text{act}} \times \frac{A_{\text{cell}}}{(30'' \times 30'')} \times (30'' \times 30'') = Sy_{\text{act}} \times A_{\text{cell}}$$

Note that the input values of kD (m^2) are not modified because the algorithm in the BCF package of MODFLOW never multiplies kD with cell dimensions.

2.4.2 Boundary conditions and recharge

No-flow boundaries were assumed at the boundaries surrounding the basin thus assuming that topographic and groundwater divides coincide. For the "big lakes" (see Fig. 1), we assumed fixed-head boundary conditions, keeping water levels constant for the entire simulation period. Here we define a "big lake" by selecting, from the f_{wat} map (see Sect. 2.2.8), only the lakes that have surface areas at least five times of $30'' \times 30''$ grid-cell. For each of those lakes, we assumed a constant water level based on the $\text{DEM}_{30''}$ of HydroSHEDS.

The monthly time series of groundwater recharge Q_{23} obtained from the land surface model of PCR-GLOBWB-MOD were fed to the "Recharge" (RCH) package of MODFLOW. The actual unit of Q_{23} is m/day. In the RCH package calculation, the input values of recharge are multiplied by the cell width and length so that they are expressed in a fluid volume per unit time (see McDonald and Harbaugh, 1988, Chapter 7), which is $m^3\,day^{-1}$ in our case. Because our MODFLOW cells have resolution $30'' \times 30''$, the input of Q_{23} must be modified as follows:

$$Q_{23,\text{inp}} = Q_{23,\text{act}} \times \frac{A_{\text{cell}}}{(30'' \times 30'')} \tag{44}$$

where $Q_{23,\text{inp}}$ is the input values that are introduced to MODFLOW and $Q_{23,\text{act}}$ are the actual values (unit: $m\,day^{-1}$) of recharge (from the land surface model output).

HESSD
8, 2555–2608, 2011

2.4.3 Channel dimensions and surface water levels

We used the "RIVER" (RIV) and "DRAIN" (DRN) packages of MODFLOW to accommodate (offline) interaction between groundwater bodies and surface water networks. Interaction between these two components are governed by actual groundwater heads and surface water levels. The latter can be translated from the monthly discharge Q_{chn} by using assumed channel properties: the channel width B_{chn} [L], channel depth D_{chn} [L], Manning roughness coefficient n [$L^{1/3} T^{-1}$], and channel longitudinal slope SI [–].

B_{chn} is derived using the formula of Lacey (1930) that postulates the width of a natural channel at bankfull flow is proportional to the root of the discharge. Lacey's formula is expressed as:

$$B_{chn} \approx P_{bkfl} = 4.8 \times Q_{bkfl}^{0.5} \tag{45}$$

where P_{bkfl} (unit: m) and Q_{bkfl} ($m^3 s^{-1}$) are the wetted perimeter and flow at bankfull condition, and 4.8 is a factor with unit $s^{0.5} m^{-0.5}$ (see Savenije, 2003, for details). In large natural alluvial rivers, P_{bkfl} is only slightly larger than B_{chn}. To calculate Q_{bkfl}, which as a rule of thumb occurs on average once every 1.5 years, we used the monthly time series of discharge Q_{chn} calculated from the land surface model.

D_{chn} is derived by combining the Lacey's formula with Manning's Eq. (Manning, 1891) and assuming a rectangular channel shape:

$$D_{chn} = \left(\frac{n \times Q_{bkfl}^{0.5}}{4.8 \times SI^{0.5}} \right)^{3/5} \tag{46}$$

By subtracting D_{chn} from $DEM_{30''}$, we may estimate the channel or river bed elevation, RBOT. However, due to errors in $DEM_{30''}$, some pixels may have unrealistic RBOT elevations. Here we implemented median filters with various window sizes to smooth the longitudinal profile of RBOT.

HESSD
8, 2555–2608, 2011

Given the channel properties, RBOT, n, B_{chn} and SI, the monthly water levels HRIV can be translated from the monthly discharge Q_{chn} by means of Manning's equation:

$$\text{HRIV} = \text{RBOT} + \left(\frac{n \times Q_{chn}}{B_{chn} \times SI^{0.5}}\right)^{3/5} \quad (47)$$

Furthermore, RBOT and monthly HRIV are used as the input for the RIV package, the principle of which is summarized as follows:

$$\text{QRIV} = \begin{cases} \text{CRDR} \times (\text{HRIV} - h) & \text{if } h > \text{RBOT} \\ \text{CRDR} \times (\text{HRIV} - \text{RBOT}) & \text{if } h \leq \text{RBOT} \end{cases} \quad (48)$$

where QRIV [$L^3 T^{-1}$] is the flow between the stream and aquifer, taken as positive if it is directed into the aquifer, h is the calculated actual groundwater head, and CRDR [$L^3 T^{-1}$] is the river conductance that calculated as follows:

$$\text{CRDR} = \text{BRES} \times P_{chn} \times L_{chn} \quad (49)$$

where BRES is the bed resistance (taken as 1 day), P_{chn} [L] is the channel wetted perimeter (approximated by B_{chn}) and L_{chn} [L] is the channel length in a $30'' \times 30''$ grid-cell (approximated by the cell diagonal length).

The RIV package is defined only in cells with $B_{chn} \geq 2$ m. To simulate smaller drainage elements, the DRN package is defined for all cells without RIV package:

$$\text{QDRN} = \begin{cases} \text{CRDR} \times (h - \text{DELV}) & \text{if } h > \text{DELV} \\ 0 & \text{if } h \leq \text{DELV} \end{cases} \quad (50)$$

where QDRN [$L^3 T^{-1}$] is the flow between the drainage network and stream and DELV is the median drain elevation, which is assumed to be located half meter below the surface elevation $\text{DEM}_{30''}$.

HESSD
8, 2555–2608, 2011

3 Sensitivity analysis of aquifer properties

In groundwater modeling, the transmissivity kD and storage coefficient Sc are important parameters which are also subject to large uncertainty. In this paper, which may be considered as our first attempt to model groundwater at large scales, we did not perform a full calibration yet. However, we did investigate the sensitivity of our groundwater model outcome to changing aquifer properties kD and Sc. Table 5 shows the list of scenarios that we have simulated, where we defined our reference scenario with $kD_{\mathrm{ref},1} = 100\,\mathrm{m}^2\,\mathrm{day}^{-1}$ and $Sc_{\mathrm{ref},1} = 0.25$ for sedimentary basins and $kD_{\mathrm{ref},2} = 25\,\mathrm{m}^2\,\mathrm{day}^{-1}$ and $Sc_{\mathrm{ref},2} = 0.02$ for mountainous area class. The other scenarios have different aquifer properties. As an example, the scenario "A02.0_B00.5" is the scenario with transmissivities $2 \times kD_{\mathrm{ref}}$ and storage coefficients $0.5 \times Sc_{\mathrm{ref}}$.

For the sake of simplicity, we used only one fixed output from the land surface model for all scenarios. The monthly recharge Q_{23} and surface water level HRIV time series maps are the same for all scenarios. To verify the land surface model output, we compared the modeled discharge in two stations located in the downstream parts of Rhine and Meuse. Here we used the data from the stations Lobith (Rhine) and Borgharen (Meuse). Note that the baseflow component of the modeled discharge evaluated here was Q_{bf} (from Eq. 28), not $-$(QRIV + QDRN) (from Eqs. 48 and 50, the negative sign $-$ indicates the flow direction from aquifer bodies to surface water networks). In other words, although they are by definition the same, we ignored the discrepancies between the baseflow values of the land surface model and groundwater model.

For each scenario, simulated groundwater levels or heads h^{m} are compared to piezometer data h^{d}. We have collected more than 30 000 sets of head time series from several institutions in the Netherlands, Belgium, France, Germany and Switzerland. For model evaluation, we selected a subset of over about 6000 time series which are relatively recent (after 1979) and long records exceeding 5 years that contain seasonal variations (at least there is a measurement datum for each season: winter, spring, summer and autumn). Moreover, based on the information given by the data suppliers,

HESSD
8, 2555–2608, 2011

we only selected the time series belonging to the top aquifer. Figure 7a shows the locations of selected measurement stations. Note that for measurement stations located in the same pixel, we did not upscale or average them to pixel scale because they usually have different time spans. It means that all measurement time series are at the point scale, not at the $30'' \times 30''$ as the model resolution, and our evaluation is therefore on the conservative side because of lack of scale adjustment.

To verify the model performance of each scenario specifically in every measurement station, we compared and evaluated modeled and observed head time series using several measures. First, we calculated the bias between both mean values, $\left[\bar{h}^{\mathrm{m}} - \bar{h}^{\mathrm{d}}\right]$, and the bias between both median values, $\left[h^{\mathrm{m}}_{50} - h^{\mathrm{d}}_{50}\right]$. Also, we calculated the cross-correlation coefficient R_{cor} between the model results and measurement data. The latter performance indicator, calculated without considering any lag, evaluates the timing of modeled time series to measurement time series. Finally, to evaluate the time series amplitude, we calculated the (relative) inter-quantile range error, QRE_{7525}:

$$\mathrm{QRE}_{7525} = \frac{\mathrm{IQ}^{\mathrm{m}}_{7525} - \mathrm{IQ}^{\mathrm{d}}_{7525}}{\mathrm{IQ}^{\mathrm{d}}_{7525}} \tag{51}$$

where $\mathrm{IQ}^{\mathrm{m}}_{7525}$ and $\mathrm{IQ}^{\mathrm{d}}_{7525}$ are the inter-quantile ranges of the model result and measurement data time series. While evaluating mean, median and bias, and cross-correlation and inter-quantile range error, we only used dates for which measurement data exist.

With so many observation points (over 6000 points selected), we decided to analyze all performance indicators (bias, cross-correlation and inter-quantile range error) at the sub-basin scale. We subdivided the model areas into several sub-basins, by using the local drainage direction map. Then, in each sub-basin, we calculated the sub-basin average of $\left|\bar{h}^{\mathrm{d}} - \bar{h}^{\mathrm{m}}\right|$, the sub-basin average of $\left|h^{\mathrm{d}}_{50} - h^{\mathrm{m}}_{50}\right|$, the sub-basin average of R_{cor} and the sub-basin average of $|\mathrm{QRE}_{7525}|$.

HESSD
8, 2555–2608, 2011

4 Results

Figures 5a and 5b show the river discharges calculated by the land surface model and the measurement data in two locations, respectively in Lobith (downstream of Rhine) and Borgharen (Meuse), both are in the Netherlands. The figures show that the discharge can be reasonably simulated by the model, except the summer discharge in Borgharen which is generally overestimated. This overestimation can be explained by the fact that our model did not include water extraction in Monsin, located about 25 km upstream of Borgharen, that is intended to sustain channel navigation to the Scheldt River (de Wit, 2001).

Some examples of comparison of simulated head time series to measurement data are presented in Fig. 5c–5g. Here, instead of plotting actual head h^{m} and h^{d} values, we plotted the model results and measurement data in their anomalies related to their mean values, $\bar{h}^{m}$ and $\bar{h}^{d}$. Note that, while calculating $\bar{h}^{m}$ and $\bar{h}^{d}$, we only used the dates for which measurement data exist. For these examples, the model is able to capture both the timing and the amplitude of observed heads quite well.

An alternative straightforward way to evaluate the model outcome is by making scatter-plots between both mean values, $\bar{h}^{d}$ and $\bar{h}^{m}$ – as shown in Fig. 6a, and between both medians, h^{d}_{50} and h^{m}_{50} – as shown in Fig. 6b. From both scatter-plots, we see that model result average and median values correlate very well to measurement data average and median values. However, these scatter-plots should be carefully interpreted because they do not provide information about the spatial distribution of biases between the model results and measurement data. Moreover, such scatter-plots are pre-dominantly influenced to areas with high densities in measurement stations, which are mainly in the lowland and valley areas of the basins. Also, some data suppliers supplied enormous number of data, while some of them supplied only few points (see Fig. 7). Areas with sparse measurement stations may not be well-represented in the scatter-plots.

HESSD
8, 2555–2608, 2011

The uneven station location distribution is another reason why we performed the analyses at the sub-basin scale. For example, Fig. 8 shows the sub-basin-scale mean absolute biases ($\left|\bar{h}^{\mathrm{d}} - \bar{h}^{\mathrm{m}}\right|$) of the reference scenario A01.0_B01.0. Here we observe that there are large biases in some sub-basins. Explanations for these biases are model structure errors (e.g. only a single layer aquifer model used), parameter errors (e.g. no calibration and only homogeneous aquifer properties used) and discrepancies in scale and reference between our model results and point measurement data. Related to the latter, we acknowledged that we did not do perform any correction to the DEM and station elevation information provided by data suppliers, who do not use the same elevation reference. This issue may be considered as one of the limitations of the current modeling approach. However, given the nature of a large-scale groundwater model, which covers multiple basins and countries, we have to accept that it is still difficult to define the same and consistent elevation reference for the whole model area. Moreover, the accuracy of the $\mathrm{DEM}_{30''}$ of HydroSHEDS used, which is the most recent derivation product of SRTM mission (http://www2.jpl.nasa.gov/srtm/), should be considered limiting since the standard accuracy value targeted in the SRTM product specification is 16 m. In MODFLOW, an accurate DEM is important for calculating actual groundwater heads h, particularly because it is needed to define drainage bed (RBOT and DELV) and surface water level (RBOT) elevations, which serve as the model boundary conditions by means of RIV and DRN packages (see Eqs. 47, 48, and 50).

Figures 9 and 10 show the sub-basin scale averages of $R_{\mathrm{cor,lag}} = 0$, which indicates the timing punctuality, and $\left|\mathrm{IQ}^{\mathrm{d}}_{7525}\right|$, which indicates the magnitude of amplitude error. Both figures present results from several scenarios with different aquifer properties (kD and Sc). We see that mostly the amplitude error $\left|\mathrm{IQ}^{\mathrm{d}}_{7525}\right|$ (Fig. 10) is sensitive to different aquifer properties, while the timing agreement $R_{\mathrm{cor,lag=0}}$ (Fig. 9) is less sensitive. The latter may be due to the fact that, although we varied kD and Sc for our MODFLOW groundwater model input, we used the same land surface model output (the

HESSD
8, 2555–2608, 2011

same recharge and surface water levels time series) for all scenarios. It seems that, to achieve better time series timing, we should have extended our sensitivity analysis by also looking at the uncertainty of our land surface model outcome. The sensitivity of $|QRE_{7525}|$ and the insensitivity of $R_{cor,lag=0}$ to the aquifer properties variation are obvious from Table 5, that summarizes the (entire) basin-scale average values for each scenario. Note that to calculate these basin-scale average values, we used the surface areas of sub-basins as weight factors. From our sensitivity analysis, we see that the basin-scale average value of $|QRE_{7525}|$ varies from 80% to above 450%, while the basin-scale average value of $R_{cor,lag=0}$ varies only from 32% to 43%.

Yet, despite the aforementioned limitation of the current sensitivity analysis, we can still observe that our groundwater model can reasonably reproduce the time series of observed groundwater head time series. Figures 11a and 11b show the histogram of the maximum values of $R_{cor,lag=0}$ and the minimum values of $\left|IQ^{d}_{7525}\right|$ that are selected from the sub-basin scale values of all scenarios (from Figs. 9 and 10). We observed that more than 50% of sub-basins have relatively good timing agreements $R_{cor,lag=0} > 0.5$, and more than 50% of sub-basins have relatively small amplitude errors $\left|IQ^{d}_{7525}\right| < 50\%$. They include not only shallow water table areas, but also areas that have deep water table (see also the lower right corner figures of Figs. 9 and 10). These facts indicate that the results of our current model are promising.

5 Conclusions and discussion

This study shows that it is possible to build a simple and reasonably accurate large-scale groundwater model by using only global datasets, suggesting a promising prospect for large-scale groundwater modeling practice, including in data-poor environments. Although the model may not be suitable for karstic aquifer areas – for which MODFLOW is not suitable for modeling groundwater flow – PCR-GLOBWB-MOD can

HESSD
8, 2555–2608, 2011

be applied in several areas that contain large sedimentary basins or pockets, such as the basins of Nile, Danube, Mekong, Yellow and Ganges-Brahmaputra Rivers.

This success also open an opportunity to improve common existing global large-scale hydrological models, such as the original version of PCR-GLOBWB (Van Beek and Bierkens, 2009), WASMOD-M (Widén-Nilsson et al., 2007) and VIC (Liang et al., 1994), which do not incorporate any lateral flows in their groundwater compartments. Although lateral groundwater flows may not be important for current common global hydrological models, which usually have a spatial resolution of 25–50 km, their inclusion may be relevant for future global hydrological models that may have spatial resolutions of down to 1 km (Wood et al., 2010).

Moreover, several authors (Bierkens and van den Hurk, 2007; Fan et al., 2007; Miguez-Macho et al., 2007; Anyah et al., 2008; Miguez-Macho et al., 2008; Maxwell and Kollet, 2008; Fan and Miguez-Macho, 2010a,b) have suggested that groundwater lateral flow components can be important for regional climate conditions. For instance, Bierkens and van den Hurk (2007) have shown that rainfall persistence may be partly explained by groundwater confluence to discharge zones that remain wet throughout the year to sustain evaporation for longer periods of time. However, for our study area that has humid climate and relatively high drainage density, the importance of groundwater lateral flows to regional climate has to be confirmed. In such areas where rainfall may be mostly transferred as hillslope and channel flows, groundwater lateral flow or groundwater confluence to discharge zones may only be important during a long dry spell. This issue may still not be resolved from our current study, but we argue that any further investigation about it can be done by using a model such as presented here.

We realize that there are several weaknesses in the current approach. The most obvious one is the fact that we did not use a full coupling between the land surface model and the groundwater model parts. Consequently, the soil moisture of the first and second stores calculated by the land surface model, do not interactively correlate to groundwater heads simulated with the groundwater model. It means that it is possible that a cell has a low soil moisture content but a high groundwater table. We also limit

HESSD
8, 2555–2608, 2011

interactions between land surface and groundwater models by inactivating capillary rise from the groundwater store (which can significantly sustain soil moisture states and evaporation fluxes) and disabling direct and interactive connection between the channel flows and groundwater tables. In this current offline coupling version, groundwater table changes do not interact with discharge flows, which were prescribed based on the land surface model output only. Also, fluctuations of lake water levels are also ignored. All of these weaknesses must be addressed while building the next generation of this model that includes full coupling between the land surface model and the groundwater model parts.

In this study, the sensitivity analysis of the groundwater head output is still limited to the uncertainty of our aquifer properties in the groundwater model, not considering the uncertainty of the land surface model outcome. In a future study, we may want to extend the sensitivity analysis by running several scenarios with varying soil properties of the first and second soil stores (unsaturated zone) to produce several recharge and surface water level time series and using them to force the groundwater model. However, considering aforementioned weaknesses discussed previously, this extended sensitivity analysis may not be meaningful if we do not use the fully coupled model. In such a fully coupled model, the dynamic feedbacks between surface water levels and groundwater heads, and between soil moisture states and groundwater heads are expected to influence the behaviour of resulting groundwater head time series.

Moreover, for such a fully coupled large-scale model, model evaluation and calibration can be reasonably done by comparing the model soil moisture states and remote sensing soil moisture products, such as AMSR-E (e.g., Njoku et al., 2003) and ERS (Wagner et al., 1999), which are also available for the entire globe. By doing this, we anticipate that a large-scale groundwater model can be evaluated and calibrated without extensive head measurement data that are hardly available in other parts of the world. Thus, it allows the construction and verification of large-scale groundwater models in data-poor environments.

HESSD
8, 2555–2608, 2011

Acknowledgements. This research was funded by the Netherlands Organization for Scientific Research NWO and the Netherlands Institute for Space Research SRON. We also received the support from Deltares and Netherlands Organization for Applied Scientific Research TNO – both are in Utrecht, The Netherlands – that allowed us to use their "GRID" parallel computing system. The authors are also indebted to many institutions that have provided groundwater head measurement data for this study, such as the central portal to Data and Information of the Subsurface of The Netherlands (DINOLoket, http://www.dinoloket.nl/), the Flanders sub-soil database (DOV, http://dov.vlaanderen.be), the Wallonia Operational Directorate-General for Agriculture, Natural Resources and the Environment (DGARNE, http://environnement.wallonie.be/), the French groundwater national portal (ADES, http://www.ades.eaufrance.fr/), the Baden-Württemberg State Environment Agency (LUBW, http://www.lubw.baden-wuerttemberg.de/), the Rhineland-Palatinate State Environment Agency (LUWG Rheinland Pfalz, http://www.luwg.rlp.de/), the North Rhine Westphalia State Environment Agency (LANUV NRW, http://www.lanuv.nrw.de/) and the Bavaria State Environment Agency (Bayerisches LfU, http://www.lfu.bayern.de/), and some individuals, such as Harrie-Jan Hendricks-Franssen and Sebastian Stoll. For the discharge data, we received the data from the Global Runoff Data Centre (GRDC, Koblenz, Germany, http://grdc.bafg.de) and the Waterbase portal (http://waterbase.nl) of Rijkwaterstaat (the Dutch Directorate General for Public Works and Water Management).

References

Allen, R. G., Pereira, L. S., Raes, D., and Smith, M.: Crop evapotranspiration: Guidelines for computing crop requirements, UN-FAO, Rome, Italy, 1998. 2561, 2569, 2573

Anyah, R. O., Weaver, C. P., Miguez-Macho, G., Fan, Y., and Robock, A.: Incorporating water table dynamics in climate modeling: 3. Simulated groundwater influence on coupled land-atmosphere variability, J. Geophys. Res., 113, D07103, doi:10.1029/2007JD009087, 2008. 2587

Bergström, S.: The HBV model, in: Computer Models of Watershed Hydrology, edited by: Singh, V., Water Resources Publications, Highlands Ranch, CO, 1995. 2562

HESSD

8, 2555–2608, 2011

Bierkens, M. F. P. and van den Hurk, B. J. J. M.: Groundwater convergence as a possible mechanism for multi-year persistence in rainfall, Geophys. Res. Lett., 34, L02402, doi:10.1029/2006GL028396, 2007. 2587
Campbell, G.: A simple method for determining unsaturated conductivity from moisture retention data, Soil Sci., 117, 311–314, 1974. 2565
Clapp, R. B. and Hornberger, G. M.: Empirical equations for some soil hydraulic properties, Water Resour. Res., 14, 601–604, 1978. 2565
D'Agnese, F. A., Faunt, C. C., Hill, M. C., and Turner, A. K.: Death valley regional groundwater flow model calibration using optimal parameter estimation methods and geoscientific information systems, Adv. Water Resour., 22, 777–790, 1999. 2557
de Wit, M.: Effect of climate change on the hydrology of the river Meuse, RIVM, National Institute op Public Health and the Environment, Bilthoven, The Netherlands, 2001. 2584
Dürr, H. H., Meybeck, M., and Dürr, S. H.: Lithologic composition of the Earth's continental surfaces derived from a new digital map emphasizing riverine material transfer, Global Biogeochem. Cy., 19, GB4S10, doi:10.1029/2005GB002515, 2005. 2557, 2576
Fan, Y. and Miguez-Macho, G.: A simple hydrologic framework for simulating wetlands in climate and earth system models, Clim. Dynam., 1–26, doi:10.1007/s00382-010-0829-8, 2010a. 2587
Fan, Y. and Miguez-Macho, G.: Potential groundwater contribution to Amazon evapotranspiration, Hydrol. Earth Syst. Sci., 14, 2039–2056, doi:10.5194/hess-14-2039-2010, 2010b. 2587
Fan, Y., Miguez-Macho, G., Weaver, C. P., Walko, R., and Robock, A.: Incorporating water table dynamics in climate modeling: 1. Water table observations and equilibrium water table simulations, J. Geophys. Res., 112, D10125, doi:10.1029/2006JD008111, 2007. 2587
FAO – Food and Agriculture Organization of the United Nations: Digital Soil Map of the World, Version 3.5. FAO, Rome, Italy, 1995. 2557, 2565, 2594, 2595
Global Soil Data Task: Global Soil Data Products CD-ROM (IGBP-DIS), 2000. 2565
Hagemann, S.: An improved land surface parameter dataset for global and regional climate models, Max-Planck-Institut für Meteorologie, Hamburg, Germany, 2002. 2561, 2594, 2595
Hagemann, S. and Gates, L. D.: Improving a subgrid runoff parameterization scheme for climate models by the use of high resolution data derived from satellite observations, Clim. Dynam., 21, 349–359, 2003. 2562, 2564
Howard, A.: A detachment-limited model of drainage basin evolution, Water Resour. Res., 30, 2261–2285, 1994. 2567

HESSD
8, 2555–2608, 2011

Kraaijenhoff van de Leur, D.: A study of non-steady groundwater flow with special reference to a reservoir coefficient, De Ingénieur, 70, 87–94, 1958. 2570

Lacey, G.: Stable channels in alluvium, Proceedings of the Institution of Civil Engineers, London, 229, 259–292, 1930. 2559, 2580

Lam, A., Karssenberg, D., van den Hurk, B. J. J. M., and Bierkens, M. F. P.: Spatial and temporal connections in groundwater contribution to evaporation, Hydrol. Earth Syst. Sci. Discuss., 8, 1541–1568, doi:10.5194/hessd-8-1541-2011, 2011. 2557

Lehner, B. and Döll, P.: Development and validation of a global database of lakes, reservoirs and wetlands, J. Hydrol., 296, 1–22, 2004. 2571

Lehner, B., Verdin, K., and Jarvis, A.: New global hydrography derived from spaceborne elevation data, Eos, 89, 2008. 2566, 2573, 2594

Liang, X., Lettenmaier, D. P., Wood, E. F., and Burges, S. J.: A simple hydrologically based model of land surface water and energy fluxes for general circulation models, J. Geophys. Res., 99, 14415–14428, 1994. 2587

Manning, R.: On the flow of water in open channels and pipes, Transactions of the Institution of Civil engineers of Ireland, 20, 161–207, 1891. 2580

Maxwell, R. M. and Kollet, S. J.: Interdependence of groundwater dynamics and land-energy feedbacks under climate change, Nat. Geosci., 1, 665–669, doi:10.1038/ngeo315, 2008. 2587

McDonald, M. and Harbaugh, A.: A modular three-dimensional finite-difference ground-water flow model: Techniques of Water-Resources Investigations of the United States Geological Survey, Book 6, http://pubs.water.usgs.gov/twri6a1 (last access: 28 February 2011), 1988. 2559, 2578, 2579, 2599

Miguez-Macho, G., Fan, Y., Weaver, C. P., Walko, R., and Robock, A.: Incorporating water table dynamics in climate modeling: 2. Formulation, validation, and soil moisture simulation, J. Geophys. Res., 112, D13108, doi:10.1029/2006JD008112, 2007. 2587

Miguez-Macho, G., Li, H., and Fan, Y.: Simulated Water Table and Soil Moisture Climatology Over North America, B. Am. Meteorol. Soc., 89, 663–672, doi:10.1175/BAMS-89-5-663, 2008. 2587

Mitchell, T. D. and Jones, P. D.: An improved method of constructing a database of monthly climate observations and associated high-resolution grids, Int. J. Climatol., 25, 693–712, 2005. 2558, 2572

HESSD

8, 2555–2608, 2011

Montgomery, D. and Foufoula-Georgiou, E.: Channel network source representation using digital elevation models, Water Resour. Res., 29, 3925–3934, 1993. 2566
New, M., Hulme, M., and Jones, P.: Representing Twentieth-Century Time Climate Variability, Part I: Development of a 1961–90 Mean Monthly Terrestrial Climatology, J. Climate, 12, 829–856, 1999. 2573
New, M., Lister, D., Hulme, M., and Makin, I.: A high-resolution data set of surface climate over global land areas, Clim. Res., 21, 1–25, 2002. 2558, 2561, 2572
Njoku, E. G., Jackson, T. J., Lakshmi, V., Chan, T. K., and Nghiem, S. V.: Soil moisture retrieval from AMSR-E, IEEE T. Geosci. Remote, 41, 215–229, 2003. 2588
Olson, J.: Global ecosystem framework-definitions, Tech. rep., USGS EROS Data Center Internal Report, Sioux Falls, SD, 1994a. 2561
Olson, J.: Global ecosystem framework-translation strategy, Tech. rep., USGS EROS Data Center Internal Report, Sioux Falls, SD, 1994b. 2561
Rodell, M., Velicogna, I., and Famiglietti, J. S.: Satellite-based estimates of groundwater depletion in India, Nature, 460, 999–1002, 2009. 2556
Rodriguez-Iturbe, I. and Rinaldo, A.: Fractal River Basins: Chance and Self-Organization, Cambridge University Press, 1997. 2567
Savenije, H. H. G.: The width of a bankfull channel; Lacey's formula explained, J. Hydrol., 276, 176–183, 2003. 2580
Savenije, H. H. G.: The importance of interception and why we should delete the term evapotranspiration from our vocabulary, Hydrol. Process., 18, 1507–1511, 2004. 2560
Sloan, P. G. and Moore, I. D.: Modeling subsurface stormflow on steeply sloping forested watersheds, Water Resour. Res., 20, 1815–1822, 1984. 2566
Snepvangers, J., Minnema, B., Berendrecht, W., Vermeulen, P., Lourens, A., van der Linden, W., Duijn, M., van Bakkel, J., Zaadnoordijk, W.-J., Boerefijn, M., Meeuwissen, M., and Lagendijk, V.: MIPWA : Water managers develop their own high-resolution groundwater model tools, in: ModelCARE 2007 : 5th International Conference on Calibration and Reliability in Groundwater Modelling Credibility of Modelling, Copenhagen, 9–13 September 2007, Prepublished Proceedings, volume 2, 108–113, 2007. 2557
Uppala, S. M., Kallberg, P. W., Simmons, A. J., Andrae, U., Bechtold, V. D., Fiorino, M., Gibson, J. K., Haseler, J., Hernandez, A., Kelly, G. A., Li, X., Onogi, K., Saarinen, S., Sokka, N., Allan, R. P., Andersson, E., Arpe, K., Balmaseda, M. A., Beljaars, A. C. M., Van De Berg, L., Bidlot, J., Bormann, N., Caires, S., Chevallier, F., Dethof, A., Dragosavac, M., Fisher,

HESSD
8, 2555–2608, 2011

M., Fuentes, M., Hagemann, S., Holm, E., Hoskins, B. J., Isaksen, L., Janssen, P. A. E. M., Jenne, R., McNally, A. P., Mahfouf, J. F., Morcrette, J. J., Rayner, N. A., Saunders, R. W., Simon, P., Sterl, A., Trenberth, K. E., Untch, A., Vasiljevic, D., Viterbo, P., and Woollen, J.: The ERA-40 re-analysis, http://edoc.mpg.de/256471 (last access: 28 February 2011), 2005. 2558, 2572

Van Beek, L.: Forcing PCR-GLOBWB with CRU data, Tech. rep., Department of Physical Geography, Utrecht University, Utrecht, The Netherlands, http://vanbeek.geo.uu.nl/suppinfo/vanbeek2008.pdf (last access: 28 February 2011), 2008. 2570, 2573, 2574, 2575, 2576, 2595

Van Beek, L. and Bierkens, M.: The Global Hydrological Model PCR-GLOBWB: Conceptualization, Parameterization and Verification, Tech. rep., Department of Physical Geography, Utrecht University, Utrecht, The Netherlands, http://vanbeek.geo.uu.nl/suppinfo/vanbeekbierkens2009.pdf (last access: 28 February 2011), 2009. 2558, 2559, 2563, 2565, 2568, 2587, 2595, 2599

Wada, Y., van Beek, L. P. H., van Kempen, C. M., Reckman, J. W. T. M., Vasak, S., and Bierkens, M. F. P.: Global depletion of groundwater resources, Geophys. Res. Lett., 37, L20402, doi:10.1029/2010GL044571, 2010. 2556

Wagner, W., Lemoine, G., and Rott, H.: A method for estimating soil moisture from ERS Scatterometer and soil data, Remote Sens. Environ., 70, 191–207, 1999. 2588

Wesseling, C. G., Karssenberg, D., van Deursen, W. P. A., and Burrough, P. A.: Integrating dynamic environmental models in GIS: The development of a Dynamic Modelling language, Transact. GIS, 1, 40–48, 1996. 2559

Widén-Nilsson, E., Halldin, S., and Yu Xu, C.: Global water-balance modelling with WASMOD-M: Parameter estimation and regionalisation, J. Hydrol., 340, 105–118, 2007. 2587

Wolf, J., Barthel, R., and Braun, J.: Modeling Ground Water Flow in Alluvial Mountainous Catchments on a Watershed Scale, Ground Water, 46, 695–705, 2008. 2577

Wood, E. F., Roundy, J. K., Troy, T. J., van Beek, L. P. H., Bierkens, M. F. P., Blyth, E., de Roo, A., Döll, P., Ek, M., Famiglietti, J., Gochis, D., van de Giesen, N., Houser, P., Jaffe, P., Kollet, S., Lehner, B., Lettenmaier, D. P., Peters-Lidard, C., Sivapalan, M., Sheffield, J., Wade, A., and Whitehead, P.: Hyper-Resolution Global Land Surface Modeling: Meeting a Grand Challenge for Monitoring Earth's Terrestrial Water, Water Resour. Res., in press, 2010. 2587

Zevenbergen, L. and Thorne, C.: Quantitative analysis of land surface topography, Earth Surf. Proc. Land., 12, 47–56, 1987. 2566

HESSD

8, 2555–2608, 2011

Table 1. List of model parameters used in the model.

Symbol	Description	Source or estimation method	Values	Unit
β	empirical exponent in the soil water retention curve	FAO soil map (1995)[a]	distributed	–
b	sub-grid elevation parameter	Equation (10)	distributed	–
B_{chn} and D_{chn}	channel width and depths	Equations (45) and (46)	distributed	m
BRES	river and drainage bed resistance	Best guess estimate	1	day
$C_{f,min}$ and $C_{f,max}$	minimum and maximum vegetation cover fractions	GLCC 2.0 land cover map[b]	distributed	–
CFR	refreezing rate in the snow pack	Best guess estimate	0.05	day^{-1}
CRDR	river and drainage bed conductance	Equation (49)	distributed	m^2 day6–1
CWH	liquid water holding capacity per unit snow storage *Ss*	Best guess estimate	0.10	$m\,m^{-1}$
DDF	degree-day factor in the snow pack	Best guess estimate	0.0055	$K\,m\,day^{-1}$
DEM	elevation value from the digital elevation map/model	HydroSHEDS (Lehner et al., 2008)	distributed	m
f_i	a parameter updating $E_{p,0}$ after interception flux	Best guess estimate	1	–
h_{veg}	vegetation height	GLCC 2.0 land cover map[c]	distributed	m
I_{nv} and I_{veg}	interception capacities per unit surface area in non vegetated and vegetated areas	Best guess estimate	0.001	m
J	groundwater recession coefficient	Equation (28)	distributed	day^{-1}
Kc_i, Kc_{wat} and Kc_s	crop factors for wet interception, surface water and bare soil areas	Best guess estimate	1	–
Kc_T	crop factor for vegetation area	Equation (26)	distributed,	–
	based on the land cover type		monthly varying	
kD	transmissivity	Best guess estimate	Sections 2.4.1 and 3	$m^2\,day^{-1}$
$k_{sat,1}$ and $k^d_{sat,2}$	saturated hydraulic conductivities	FAO soil map (1995)	distributed	$m\,day^{-1}$
L	hillslope length	DEM of HydroSHEDS	distributed	m
LAI_{min} and LAI_{max}	minimum and maximum leaf area indexes	Table of Hagemann (2002)	distributed	–
n	Manning coefficient	Best guess estimate	0.045	$m^{1/3}\,s^{-1}$

HESSD
8, 2555–2608, 2011

Table 1. Continued.

Symbol	Description	Source or estimation method	Values	Unit
$\psi_{50\%}$	soil matric suction at which transpiration is halved	Best guess estimate	3.33	m
ψ_{fc}	soil matric suction at field capacity	Best guess estimate	1	m
$\psi_{sat,1}$ and $\psi_{sat,2}$	soil matric suctions at saturation	FAO soil map (1995)	distributed	m
SC_1 and SC_2	soil water storage capacities	$(\psi_{sat,1} \times Z_1)$ and $(\psi_{sat,2} \times Z_2)$	distributed	m
RBOT and DELV	river bed and drain elevations	Section 2.4.3	distributed	m
Si_{max}	interception capacity	Equation (1)	distributed, monthly varying	m
Sl	channel longitudinal slope	DEM of HydroSHEDS	distributed	–
Sy	aquifer porosity or storage coefficient or specific yield	Best guess estimate	Sections 2.4.1 and 3	–
$\theta_{sat,1}$ and $\theta_{sat,2}$	effective soil moisture contents at saturation	FAO soil map (1995)	distributed	m day^{-1}
$\tan(\alpha)$	grid-average slope	DEM of HydroSHEDS	distributed	–
T_{LR}	temperature lapse rate	Best guess estimate	−0.65	K m−1
W_{max}	grid-average soil storage	$SC_1 + SC_2$	distributed	m
W_{min}	grid-minimum soil storage	Best guess estimate	0	m
Z_1 and Z_2	soil thicknesses	FAO soil map (1995)	distributed	m

[a] The parameterization of FAO map (1995) based on Table of Van Beek and Bierkens (2009).

[b] The parameterization of GLCC 2.0 land cover map based on Table of Hagemann (2002).

[c] The parameterization of the vegetation height h_{veg} based on Table of Van Beek (2008).

[d] The subscripts 1 and 2 indicate the first and second soil storages.

HESSD
8, 2555–2608, 2011

Table 2. List of state and flux variables defined in the models.

Symbol	Description	Unit
d_{gw}	groundwater depth = DEM$-h$	m
E_i	evaporation flux from the intercepted water	m day^{-1}
$E_{p,0}$	reference potential evaporation energy (forcing data)	m day^{-1}
$E_{p,i}$	potential evaporation energy for wet interception areas	m day^{-1}
$E_{p,s}$	potential evaporation energy for bare soil areas	m day^{-1}
Es	total soil evaporation = $Es_1 + Es_l$	m day^{-1}
Es_1	soil evaporation from the first soil store	m day^{-1}
Es_l	soil evaporation from the melt water store in the snow pack	m day^{-1}
E_{wat}	surface water evaporation	m day^{-1}
h	groundwater head	m
HRIV	monthly surface water levels/elevations	m
$k_1(s_1)$ and $k_2(s_2)$	hydraulic conductivities at specific degree of saturations s_1 and s_2^*	m day^{-1}
s_1 and s_2	degrees of saturation (S_1/SC_1 and S_2/SC_2)	m
$\psi_1(s_1)$ and $\psi_2(s_2)$	soil matric suctions (at specific degree of saturations s_1 and s_2)	m
P	total precipitation (forcing data)	m day^{-1}
P_{01}	infiltration flux to the first soil layer	m day^{-1}
P_n	net precipitation flux transferred to the soil	m day^{-1}
P_{rain}	liquid rainfall flux	m day^{-1}
Q_{12} and Q_{23}	net percolation fluxes from the first to second soil layers = $Q_{1\to2} + Q_{2\to1}$; and from the second soil layer to groundwater storage = $Q_{2\to3} + Q_{3\to2}$	m day^{-1}
$Q_{1\to2}$ and $Q_{2\to3}$	downward components of percolation fluxes, from the first to second soil stores and from the second to groundwater stores	m day^{-1}
$Q_{2\to1}$ and $Q_{3\to2}$	Upward seepage (capillary rise) fluxes, from the second to first soil stores and from the third groundwater to second stores. For this study, the latter is inactivated ($Q_{3\to2} = 0$).	m day^{-1}
Q_{bf}	baseflow	m day^{-1}
Q_{chn}	monthly average discharge from the land surface model output	m^3 s^{-1}
Q_{dr}	direct runoff	m day^{-1}
Q_{sf}	interflow or shallow sub-surface flow	m day^{-1}
Q_{tot}	total local runoff expressed as a fluid volume per unit time	m^3 day^{-1} or m^3 s^{-1}
Q_{wat}	change in surface water storage	m day^{-1}
S_1 and S_2	pper soil storages (first and second soil storages)	m
S_3	groundwater storage	m
Si	interception storage	m
Sn	snow flux	m day^{-1}
Ss	snow storage	m
Ss_l	melt water storage in the snow pack	m
t and Δt	time and timestep	day
Ta	atmospheric temperature (forcing data)	˚C or K
W_{act}	grid-average actual soil storage (Improved Arno Scheme) = $S_1 + S_2$	m
x	fraction of saturated soil	–

* The subscripts 1 and 2 indicate the first and second soil storages.

HESSD
8, 2555–2608, 2011

Table 3. List of sensitivity analysis scenarios including their performance indicator values.

Scenarios	Transmissivities kD	Storage coefficients Sc	$R_{cor,lag} = 0$	QRE_{7525}
A00.5_B00.1	$0.5 \times kD_{ref}$	$0.1 \times Sc_{ref}$	NA	NA
A00.5_B00.2	$0.5 \times kD_{ref}$	$0.2 \times Sc_{ref}$	NA	NA
A00.5_B00.3	$0.5 \times kD_{ref}$	$0.3 \times Sc_{ref}$	0.42	254%
A00.5_B00.5	$0.5 \times kD_{ref}$	$0.5 \times Sc_{ref}$	0.40	190%
A00.5_B01.0	$0.5 \times kD_{ref}$	$1 \times Sc_{ref}$	0.36	133%
A00.5_B02.0	$0.5 \times kD_{ref}$	$2.0 \times Sc_{ref}$	0.33	103%
A01.0_B00.1	$1 \times kD_{ref}$	$0.1 \times Sc_{ref}$	NA	NA
A01.0_B00.2	$1 \times kD_{ref}$	$0.2 \times Sc_{ref}$	0.43	352%
A01.0_B00.3	$1 \times kD_{ref}$	$0.3 \times Sc_{ref}$	0.42	276%
A01.0_B00.5	$1 \times kD_{ref}$	$0.5 \times Sc_{ref}$	0.40	203%
A01.0_B01.0 (reference)	$1 \times kD_{ref}$	$1 \times Sc_{ref}$	0.36	138%
A01.0_B02.0	$1 \times kD_{ref}$	$2 \times Sc_{ref}$	0.32	103%
A02.0_B00.1	$2 \times kD_{ref}$	$0.1 \times Sc_{ref}$	NA	NA
A02.0_B00.2	$2 \times kD_{ref}$	$0.2 \times Sc_{ref}$	0.43	339%
A02.0_B00.3	$2 \times kD_{ref}$	$0.3 \times Sc_{ref}$	0.42	261%
A02.0_B00.5	$2 \times kD_{ref}$	$0.5 \times Sc_{ref}$	0.40	188%
A02.0_B01.0	$2 \times kD_{ref}$	$1 \times Sc_{ref}$	0.36	128%
A02.0_B02.0	$2 \times kD_{ref}$	$2 \times Sc_{ref}$	0.32	98%
A05.0_B00.1	$5 \times kD_{ref}$	$0.1 \times Sc_{ref}$	0.43	472%
A05.0_B00.2	$5 \times kD_{ref}$	$0.2 \times Sc_{ref}$	0.43	313%
A05.0_B00.3	$5 \times kD_{ref}$	$0.3 \times Sc_{ref}$	0.42	242%
A05.0_B00.5	$5 \times kD_{ref}$	$0.5 \times Sc_{ref}$	0.40	176%
A05.0_B01.0	$5 \times kD_{ref}$	$1 \times Sc_{ref}$	0.36	116%
A05.0_B02.0	$5 \times kD_{ref}$	$2 \times Sc_{ref}$	0.32	89%
A10.0_B00.1	$10 \times kD_{ref}$	$0.1 \times Sc_{ref}$	0.43	437%
A10.0_B00.2	$10 \times kD_{ref}$	$0.2 \times Sc_{ref}$	0.42	291%
A10.0_B00.3	$10 \times kD_{ref}$	$0.3 \times Sc_{ref}$	0.41	222%
A10.0_B00.5	$10 \times kD_{ref}$	$0.5 \times Sc_{ref}$	0.40	160%
A10.0_B01.0	$10 \times kD_{ref}$	$1 \times Sc_{ref}$	0.37	110%
A10.0_B02.0	$10 \times kD_{ref}$	$2 \times Sc_{ref}$	0.33	84%

* NA indicates the scenarios that failed to converge, specifically the ones with low transmissivities and storage coefficients.

HESSD
8, 2555–2608, 2011

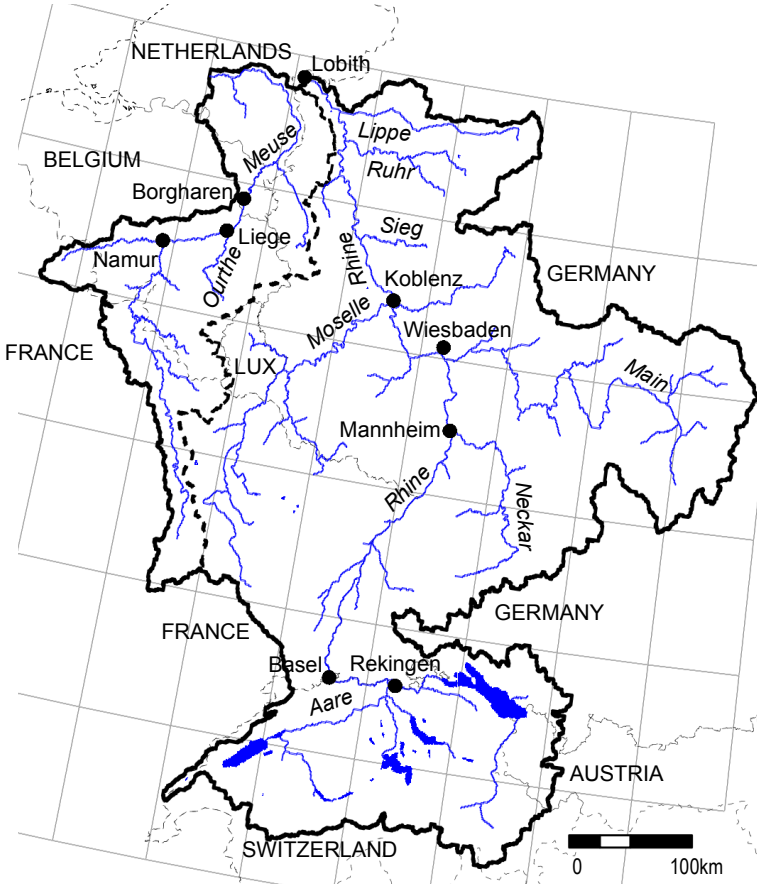

Fig. 1. The combined Rhine-Meuse basin used as the test bed for this model. The bold black line indicates the scope of the model area while the bold dashed line indicates the approximate border between the Meuse and Rhine basins. The major rivers and big lakes are indicated in blue.

HESSD
8, 2555–2608, 2011

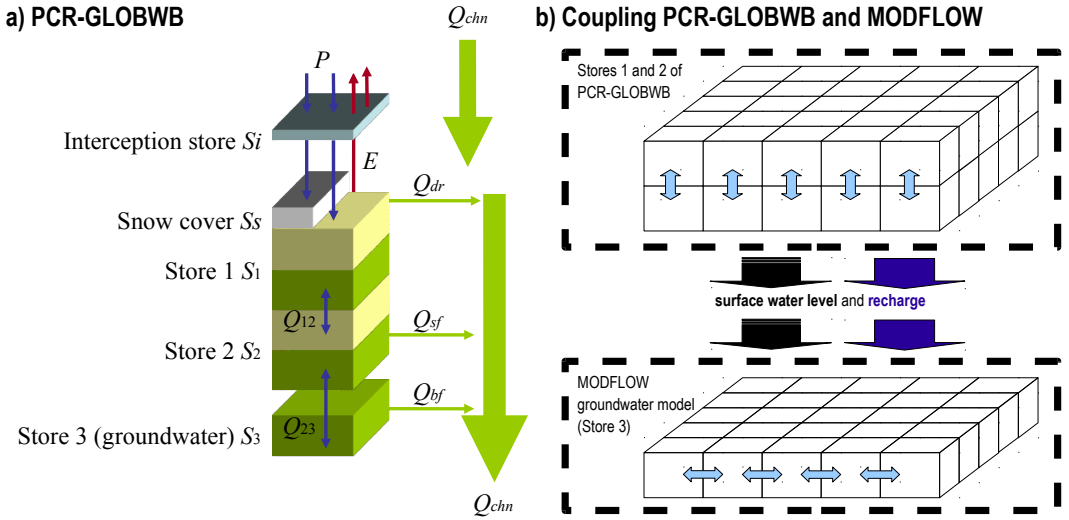

Fig. 2. The modeling structure and strategy for this study: **(a)** the concept of the land surface model of PCR-GLOBWB (Van Beek and Bierkens, 2009): on the left, the soil compartment, divided in the two upper soil stores, S_1 and S_2, and the linear groundwater store, S_3, that is replaced by the MODFLOW (McDonald and Harbaugh, 1988) groundwater model. On the right, the total local gains from all cells are routed along the local drainage direction to yield the channel discharge, Q_{chn}. **(b)** The modeling strategy used to couple the PCR-GLOBWB and MODFLOW: First, we run the PCR-GLOBWB to calculate net recharge Q_{23} to groundwater store and channel discharge Q_{chn} that can be translated into surface water levels by assuming channel dimensions. Then, the monthly net recharge and surface water levels are used to force MODFLOW.

HESSD
8, 2555–2608, 2011

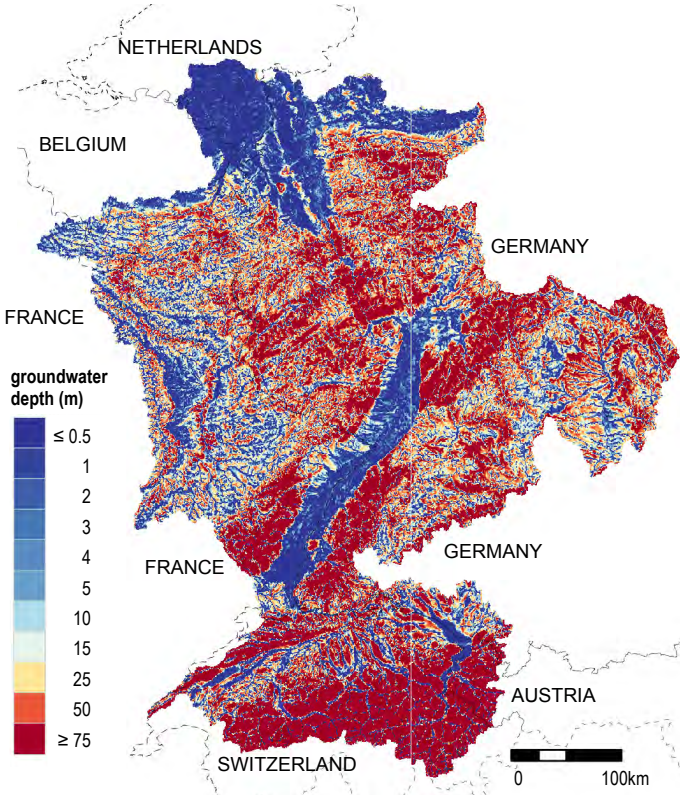

Fig. 3. The approximate steady-state groundwater depth map that is used for aquifer classification. Here, we classified cells that have groundwater depth below 25 m and their downstream cells as the "sedimentary basin", where shallow productive aquifer pockets are usually located. Moreover, we also made sure that a sedimentary basin cell must have at least one neighboring cell in its left, right, upper, or lower extents. The remaining cells were classified as "mountainous areas", where groundwater depths are large (see Sect. 2.4.1).

HESSD
8, 2555–2608, 2011

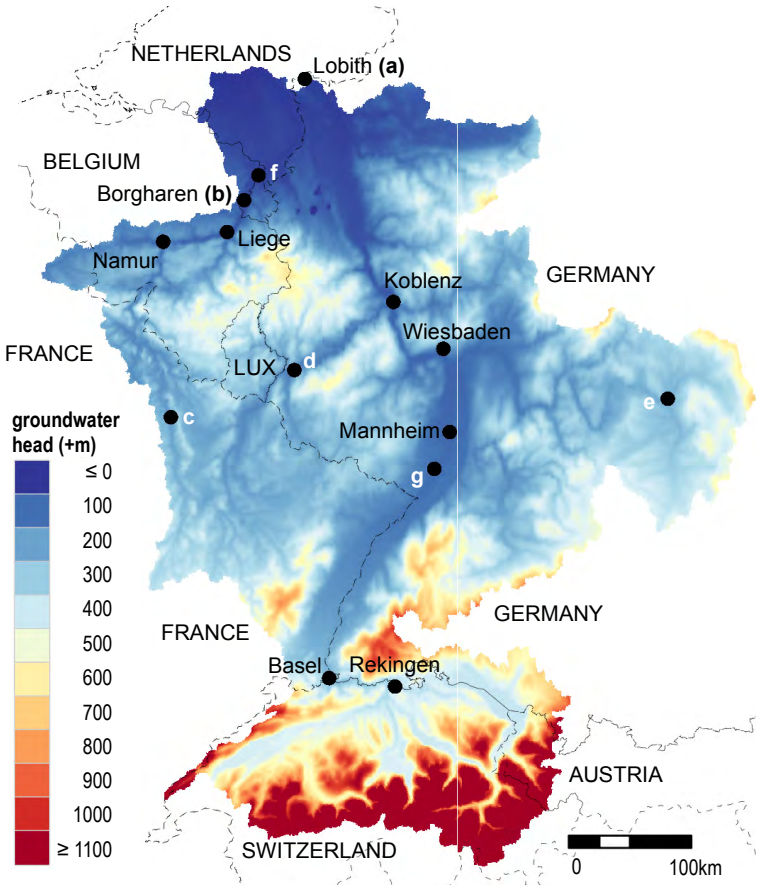

Fig. 4. The average calculated groundwater head for the period 1974–2008, based on the reference scenario A01.0_B01.0. The alphabetical codes shown on the maps indicate the measurement station locations for the graphs in Fig. 5.

HESSD
8, 2555–2608, 2011

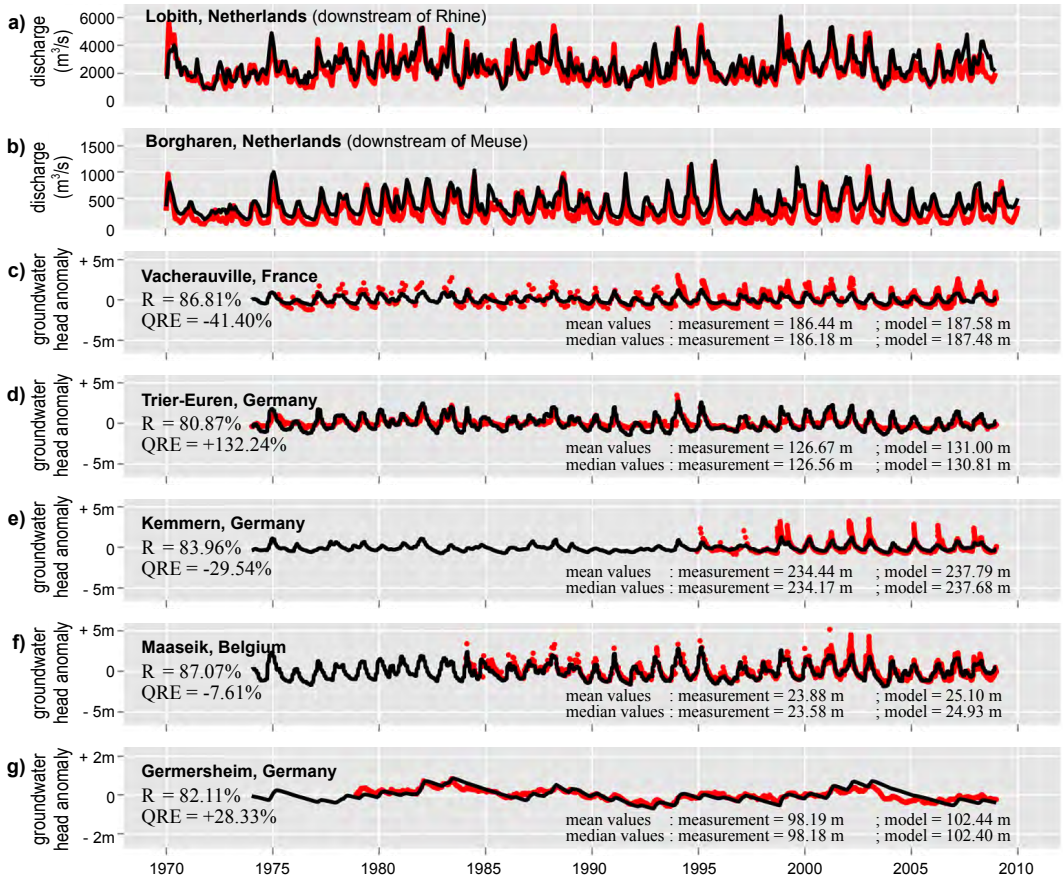

Fig. 5. The comparison between measurement data (red) and model output (black): **(a)** the discharge in Lobith, located downstream of the Rhine. **(b)** The discharge in Borgharen, located downstream of Meuse. **(c, d, e, f, and g)** Groundwater head anomaly comparisons based on the reference scenario A01.0_B01.0 at several locations indicated in Fig. 4.

HESSD
8, 2555–2608, 2011

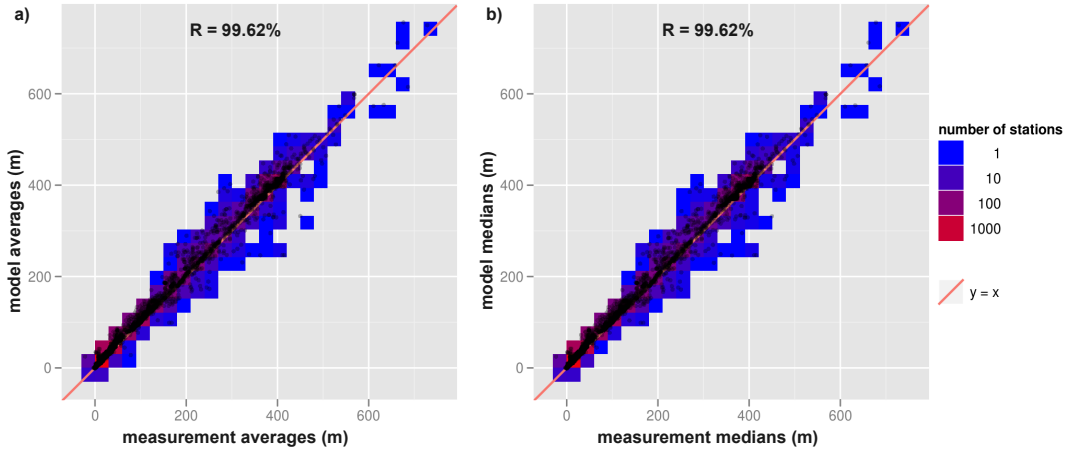

Fig. 6. The scatter-plots comparing between: **(a)** model result averages vs. measurement data averages; **(b)** model result median values vs. measurement data median values.

HESSD
8, 2555–2608, 2011

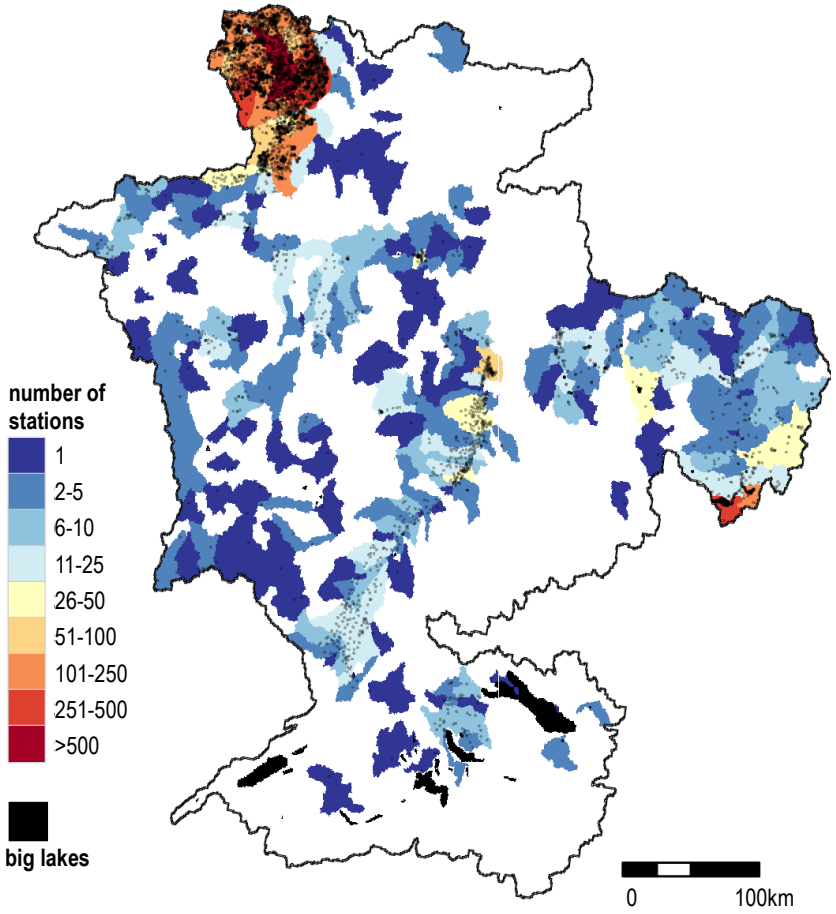

Fig. 7. The sub-basins used to analyze the model performance. The locations and number of head measurement stations in each of sub-basin is also illustrated.

HESSD
8, 2555–2608, 2011

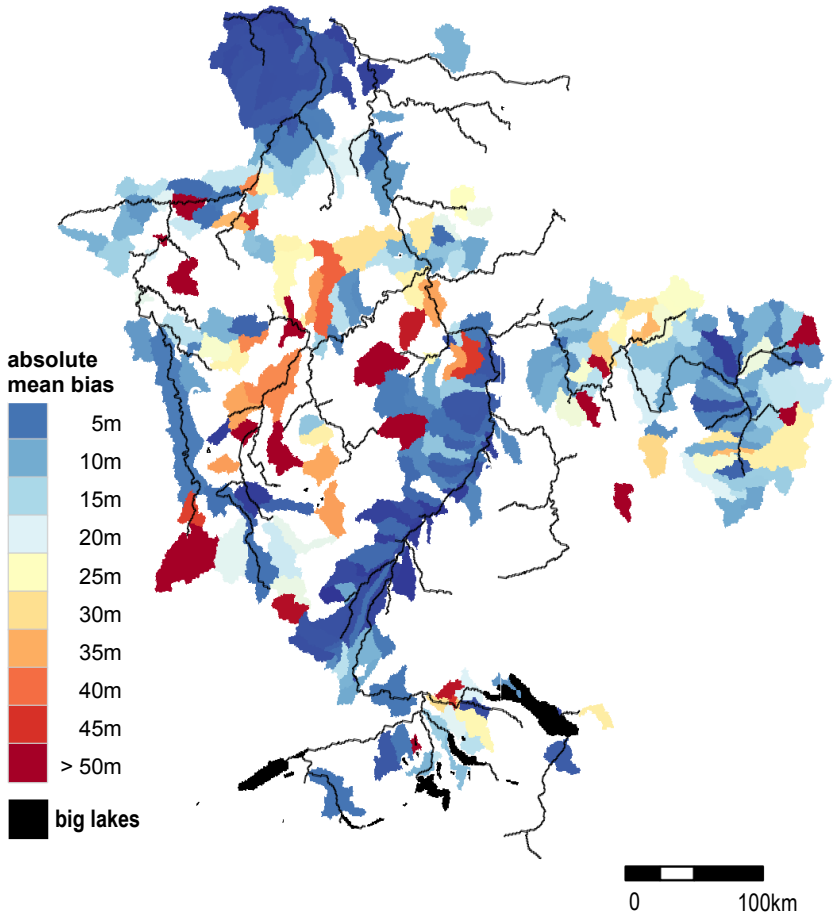

Fig. 8. The sub-basin averages of absolute mean biases, based on the reference scenario A01.0_B01.0.

HESSD
8, 2555–2608, 2011

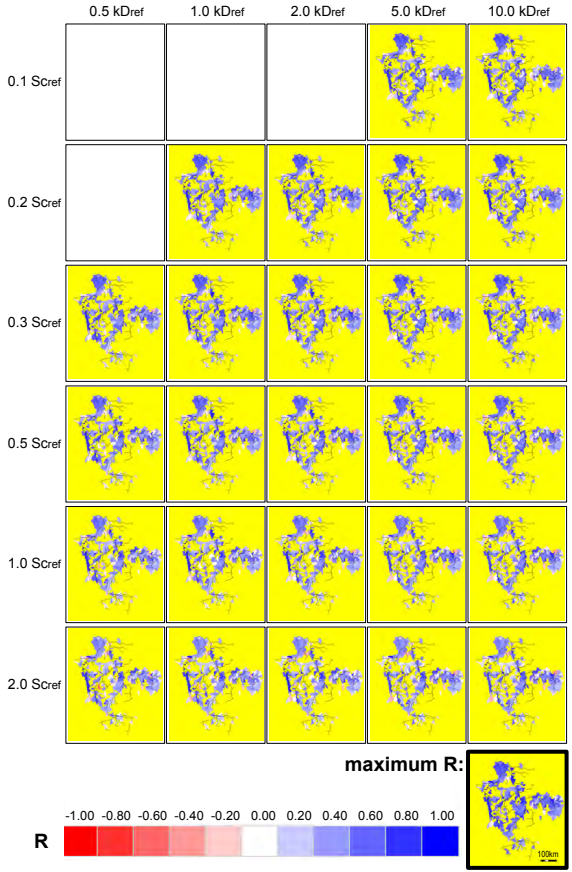

Fig. 9. The sub-basin average of timing agreement $R_{cor,lag=0}$ for all scenarios. To distinguish near zero values (white), we use a yellow background. The lower right corner map is a composite map of the maximum values of all scenarios. Note: some scenarios with small tranmissivities *kD* and storage coefficients *Sc* failed to converge.

HESSD
8, 2555–2608, 2011

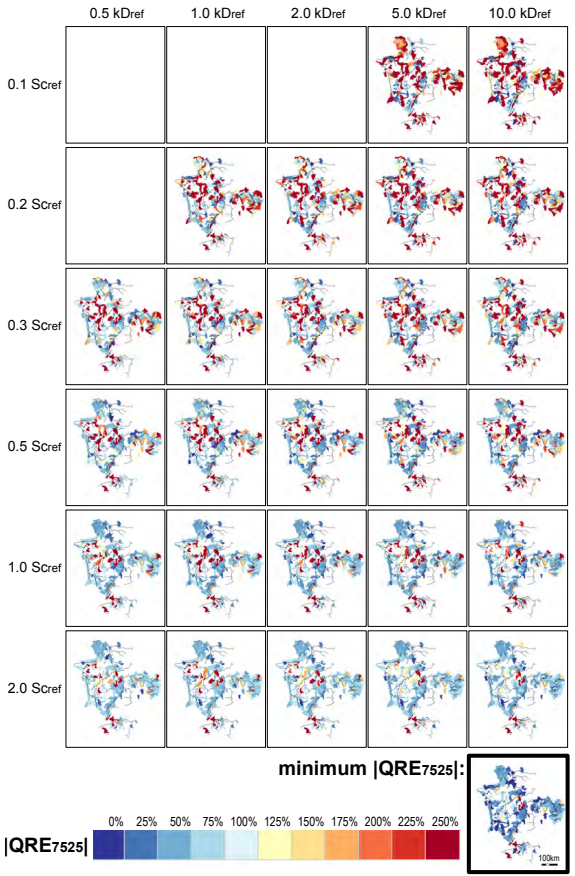

Fig. 10. The sub-basin average of amplitude error $|QRE_{7525}|$ for all scenarios. The lower right corner map is a composite map of the minimum values of all scenarios. Note: Some scenarios with small tranmissivities *kD* and storage coefficients *Sc* failed to converge.

HESSD
8, 2555–2608, 2011

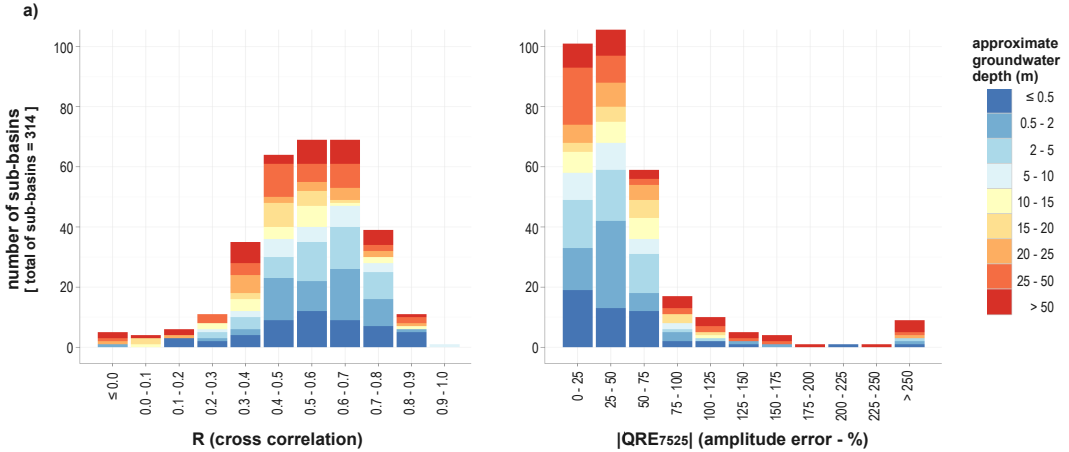

Fig. 11. Histograms of maximum values of all maps in Fig. 9 (cross correlation $R_{cor,lag=0}$) and minimum values of all maps in Fig. 10 (amplitude error $|QRE_{7525}|$). Each bar in the histogram is clustered based on approximate groundwater depths that are calculated by averaging the 34-year 1974–2008 average modeled groundwater heads of all scenarios. Note that, to calculate these average depths, we used only cells with measuring stations.

HESSD
8, 2555–2608, 2011